Continuum Modelling of Al/CuO Nanothermite Pellet Combustion

by

Joseph Mark Rodger Epps

A thesis
presented to the University of Waterloo
in fulfillment of the
thesis requirement for the degree of
Master of Applied Science
in
Mechanical and Mechatronics Engineering

Waterloo, Ontario, Canada, 2020

Author's Declaration

I hereby declare that I am the sole author of this thesis. This is a true copy of the thesis, including any required final revisions, as accepted by my examiners.

I understand that my thesis may be made electronically available to the public.

Abstract

Nanothermite mixtures are made up of nano-sized metallic fuel and inorganic oxidizer components. As this solid mixture represents a metastable intermolecular composite, an increase in nanothermite temperature can initiate a highly exothermic reaction. As the oxidation takes place at the surface of nanoparticles, the nanothermite composite is characterized by a very high reactivity compared to other type of solid propellants such as their micro-sized counterparts. Furthermore, as their geometries and molecular make up are highly tuneable, so are their burning characteristics. These characteristics are well suited for a number of engineering applications such as pyrotechnics, igniters, explosives, and propellants.

Literature contains many studies with experimental results for different nanothermite mixtures and in different setups such as consolidated pellets. Numerical studies are limited and have focused on quantifying the reaction rather than the aggregate effects of the pellet. When the nanothermite mixture of powders is pressed into a pellet form, porosity arises due to the imperfect contact between the particles. Literature does accept that burning occurs primarily due to conduction or convection; the later of which is dominant when porosity is high (lightly pressed).

This thesis will introduce a continuum method of modelling the reaction propagation mechanisms in Al/CuO nanothermite pellets following the experimental results from a previous University of Waterloo graduate student, now doctorate holder. Some researchers have undertaken meta-scale models as an attempt to simulate the pellet and its governing processes. The modelling framework here will build on this by coupling the field of porous media to capture the porosity effects of the pellet. Al/CuO generates a significant amount of gas, which will play an important role in modelling the convective heat transfer. With that said, this framework can be extended to other gas generating nanothermite reactions. Reaction details are secondary to this study, so the reaction is modelled with a simplified reaction model. A non-dimensional analysis of this model was used to identify important characteristics of combustion to process the results.

A Finite Volume Method was developed in Python to numerically solve the proposed

model and obtain results. The results show a relationship between the burn rate and Peclet number that agrees well with experimental results. Burning regimes governed by conduction and convection were confirmed to be functions of packing density, however burn rate magnitudes fell short of most literature results at low packing density. Without being able to quantify the pore structure within the pellet, there is significant uncertainty in the parameters used to calculate porous media permeability and thermal conductivity.

Acknowledgements

I would like to thank my supervisors, Drs Jean-Pierre (JP) Hickey and John Wen for giving me the opportunity to research under them. I have learned a lot about numerical modelling, coding, technical writing and combustion thanks to them.

I also want to thank the members on the committee, Drs Cecile Devaud and Jeff Gostick, for taking the time to read my thesis and provide me with feedback.

Thank you to my research colleagues over the last (almost) two years; Dr. Florin Sacheanu (before his title) and Alex Baranovski for the many discussions about experiments and modelling. To the other colleagues, Amitvikram Dutta, Khaled Younes, Victoria Kerr and Shina Maini for the many conversations about research and ensuring I remained sane; you all were more important to me than you might've realized.

Lastly, I want to thank my parents; for always being someone to talk to through the good and bad times, always supporting and believing in me. I may not have wanted mom's advice from her graduate school days all the time, but it was all for love. Talking about coding and programming experiences with Dad made me feel good about my code and also taught him some things about Python.

Table of Contents

List of Figures

List of Tables

Chapter 1

Introduction

1.1 Thermites Reactions

Thermites are found in a number of engineering applications such as pyrotechnics, igniters, explosives, and propellants. They consist of a mixture of a metal (A), often called the fuel, and a metal-oxide (BO) compound often termed the oxidizer. Metal (A) is a stronger oxidizing agent than metal (B) which makes a small amount of energy input able to initiate a chemical reaction which follows the form:

$$\mathrm{A} + \mathrm{BO} \longrightarrow \mathrm{AO} + \mathrm{B} \tag{1.1}$$

This chemical reorganization is highly exothermic and results in the formation of the stable oxide (AO) and free metal (B). The reaction is initiated by an external energy source such as a laser, hot wire, electrostatic discharge or impact.

Aluminum is a common metal fuel paired with oxidizers such as Nickel oxide (NiO), Molybdenum oxide (MoO_3), copper oxide (CuO), Bismuth oxide (Bi_2O_3) and Tungsten oxide (WO_3). Select stoichiometric equations, heat of combustion, adiabatic flame temperature and gas generation values are shown in Table 1.1.

Table 1.1: Common thermite reaction equations, heat of combustion, adiabatic flame temperature and gas generation [11]

Chemical Equation	**Enthalpy of Combustion [kJ/g]**	**Adiabatic Flame Temperature [K]**	**Gas generation [g gas/g mix]**
$2\,Al + 3\,CuO \longrightarrow Al_2O_3 + 3\,Cu$	4.076	2843	0.3431
$2\,Al + MoO_3 \longrightarrow Al_2O_3 + Mo$	4.703	3253	0.2473
$2\,Al + WO_3 \longrightarrow Al_2O_3 + W$	2.914	3253	0.1463
$2\,Al + Bi_2O_3 \longrightarrow Al_2O_3 + 2\,Bi$	2.118	3253	0.8941
$2\,Al + 3\,NiO \longrightarrow Al_2O_3 + 3\,Ni$	3.441	3187	0.0063

1.2 Fabrication and Characterization

Thermites are fabricated by mixing the desired fuel and oxidizer powders. These powders can contain particles on the nano (10 to 100 nm in diameter) or micron (>1 µm in diameter) scale. Thermites fabricated using predominantly nano-sized particles are classified as nanothermites or nanocomposites. Equivalence Ratio (ER), seen in classic gas-phase combustion, is used to state the ratio of the fuel-oxidizer mass fraction ((F/O)) in the mixture compared to the stoichiometric mass fractions amount ($(F/O)_{stoich}$):

$$ER = \frac{(F/O)}{(F/O)_{stoich}} \tag{1.2}$$

The powders are mixed with Ultrasonic Mixing, Electro-spraying or Arrested Reactive Milling. Once mixed, the particles tend to agglomerate together forming structures that approach micron scale. After mixing, they can be pressed into consolidated pellets or remain as loose powders for ignition. Each setup is characterized relative to its Theoretical Maximum Density (TMD) with tightly packed pellets being more dense and loose powders being less dense. The degree of packing results in pores being dispersed throughout the

structure. In the study of porous media, the porosity is defined as the volume fraction of pores to total volume:

$$\phi = \frac{V_{pores}}{V_{total}} \tag{1.3}$$

ϕ can be used to represent equivalence ratio in the combustion field, and it can represent the solid volume fraction (conjugate of porosity) in porous media fields, however ϕ will represent porosity in this thesis. Although a lot of terminology used in gas-phase combustion is used in the description of nanothermites, the term 'flame' is commonly associated with gas-phase combustion. Since nanothermites are a form of solid fuel, the 'flame' equivalent will be referred to as 'reaction front' and the equivalent of the 'flame speed' will be termed 'burn rate'. The concept of the adiabatic flame temperature will remain the same.

1.3 Motivation and Objectives

As the oxidation takes place at the surface of nanoparticles, the nanothermite composite is characterized by a very high reactivity compared to other type of solid propellants such as their micro-sized counterparts. Furthermore, as their geometries and molecular make up are highly tuneable, so are their burning characteristics. With the right adjustments, the reactive front propagation ranges from 1 to 1000 $\mathrm{m\,s^{-1}}$.

To find the right configuration that yields the desired combustion characteristics requires extensive understanding of what governs combustion and how that information can be applied during fabrication. The objective of this research is to numerically quantify the mechanisms governing Al/CuO nanothermite combustion. Many experimental studies have been done to quantify the dominating processes during combustion, but few numerical studies have been done. Therefore, a numerical model will be developed and analyzed to infer information about the combustion processes. The existing experimental and numerical studies (Chapter 2) will provide a foundation and couple it with the field of porous media to develop the model in Chapter 3. An in-house developed code was used to solve the model and details of the numerical implementation as well as simulation details will be described in Chapter 4. The results and discussion will be in Chapters 5 and 6 respectively.

1.4 Contributions

The major contributions of this research are:

- Develop comprehensive continuum model of nanothermite pellet combustion with a focus on the porous medium flow
- Propose a scaling analysis to quantify the governing propagation mechanisms during combustion
- An open-source code was used and is available for future researchers to use
- Model was validated and provides a foundation for further continuum models to be developed from

Chapter 2

Literature Review

Literature studies on micro and nano scale thermite reactions show different burning characteristics. Experimental and numerical studies were done on nanothermites to develop an understanding of its combustion characteristics. This section will summarize the said studies that will provide the foundation for the proposed model described in Chapter 3.

2.1 Experimental Observations

2.1.1 Burning Regimes

The burn rate in nanothermite pellet combustion ranges from 1 to 1000 $\mathrm{m\,s^{-1}}$ and has been shown to be highly dependent on the pellet packing density [26, 1, 25]. Though, the exact mechanism(s) responsible for the dramatic variation in burn rates remains subject to debate. Literature generally accepts two dominant burning regimes where the reaction propagation is governed, to varying degrees, by convection or conduction [33, 8, 25]. Being consolidated metallic pellets, conduction of heat is a natural means to advance the reactive front through nanothermite pellet; the timescale of conductive heat transfer is governed by the thermophysical properties of the material. Pores arise from the imperfect contact of the nanoparticles in compressed pellets which inhibit conduction, but promote advection

of fluid through this porous medium. The pressure-driven advection, or convection, of high temperature combustion products through the pellets is the secondary means of reactive front propagation.

Sanders et al. [26] observed decreasing burn rates with increasing packing density in Al/MoO_3 nanothermites suggesting impeded advection at higher densities. Saceleanu et al. [25] also observed a similar trend with Al/CuO pellets. Higher packing densities will have fewer and smaller pores which will favour conduction as the primary heat transfer mechanism. Weismiller et al. [33] observed decreasing burning rates with increasing ambient pressures in Al/CuO; since the pressure gradient drives the mass flow through the porous medium, increasing the ambient pressure should naturally inhibit advection. Scaling arguments done by Weismiller et al. [33] with Fourier, Darcy's and the ideal gas laws argued this supported conduction and convection as the primary propagation modes. Therefore it is clear that a combination of conduction and convection mechanisms help sustain the reaction front within a nanothermite pellet.

2.1.2 Convective Heat Transfer

In order for convective heat transfer to sustain the reaction front, a strong pressure gradient within the pellet must be generated; this pressure generation is tied to the gas formation and expansion resulting from the nanothermite oxidation. Thermite reaction calculations done by Fischer and Grubelich [11] suggest significant amounts of gas are generated during certain fuel-oxidizer combinations. Experiments in [33, 26, 7, 1] observed pressures generated for aluminum with copper, molybdenum, bismuth and tungsten oxides supporting gas generation. The source and composition of the gas has been theorized in literature with one common consensus around the decomposition of the oxidizer [31, 14]. Jian et al. [15] observed the decomposition temperatures of several oxidizers and compared them to the nanothermite ignition temperatures. It was observed that some fuel-oxidizer combinations will generate gas just before ignition, but that it is not a prerequisite for ignition. Oxidizers such as molybdenum and tungsten oxide do not decompose, so gas generation will not precede ignition. For gas generating nanothermites, the changing density caused

by the phase change can provide a source of pressure to propagate the reaction assuming the reaction is sufficiently fast.

Based on scaling arguments, Egan and Zachariah [8] suggest convective heat transfer by gases is not sufficient to support the high burn rates in less dense pellets. Convective heat transfer of condensed phases were more likely to support the higher burning rates. Furthermore, the reaction of Al/NiO generates very little gas but Dean et al. [7] still measured a significant pressure during the reaction. This is where the Melting Dispersion Mechanism (MDM) is proposed as an explanation for faster burn rates. Aluminum particles have a thin shell of alumina around them and in the MDM, this acts as a crucible for aluminum to melt inside due to its lower melting point compared to alumina. At these high temperatures, the shell ruptures due to thermal expansion, which then advects molten aluminum causing the pressure generation. First proposed numerically by Levitas et al. [19] for aluminum based thermites, further experiments done by Levitas et al. [20] found evidence of the MDM by analyzing the microstructures pre and post combustion. The theory proposed by Dean et al. [7] is that the advection of molten aluminum produces a dynamic pressure that was observed in their experiments. Sanders et al. [26] and Granier and Pantoya [13] hypothesized a similar mechanism for Al/MoO_3 experiments. The MDM supports the hypothesis by Egan and Zachariah [8] that condensed phase heat transfer can produce the burn rates observed in experiments. Therefore, pressure generation is likely caused by a combination of intermediate gaseous species during the reaction as well as advecting fluids. Also, the convective heat transfer governing less dense pellets might include condensed phases as well as gases.

2.1.3 Other Findings

Packing density thus far has been introduced as a major contributor to the reaction front propagation for the different burning regimes it creates. Other experimental studies have also looked at the effect of different fabrication methods and equivalence ratios. Granier and Pantoya [13] noted a difference in burn rates and ignition delays with different equivalence ratios. Saceleanu et al. [25] also experimented with different equivalence ratios,

however their main contribution was on packing density effects. Monk et al. [21] found that the burning characteristics of stoichiometric Al/CuO differed when prepared via Ultrasonic Mixing, Electro-spraying and Arrested Reactive Milling. After preparing with each method, they were analyzed by Scanning Electron Microscopy (SEM) before and after ignition. Ignition delay, burn time and microstructures were all found to vary based on preparation method. Park et. al. [1] used aluminum with different CuO morphologies such as nanoparticles, nanowires and microparticles which produced different burning characteristics. Fabrication and the microstructures also have impacts on the burning characteristics.

Another interesting observation about laser ignited nanothermites was the significant ablation. Both Stacy et al. [27] and Saceleanu et al. [25] observed ablation during pre-ignition heating. As the top layer is heated, it is ablated away due to a combination of thermal expansion and gas generation [27] effectively increasing the time required to heat the powders to ignition. Stacy et al. [27] found that there was a power threshold above which ablation increases and further delaying ignition of the pellet. Even Monk et al. [21] noticed significant material ablation when igniting samples with electrostatic discharge. For laser and electrostatic discharge initiated reactions, ablation is a significant phenomena that has an impact on ignition delay since it creates a discontinuity where the heat is applied and how the pellet heats up.

2.2 Numerical Studies

Efforts in modelling nanothermite combustion have been undertaken despite an incomplete understanding of the tightly coupled physical phenomena arising in this problem. Umbrajkar et al. [31], Ermoline and Schoenitz [9], and Stamatis et al. [29] attempted to model low temperature ignition using CuO decomposition and alumina phase transformation. Their reaction kinetics used 3-4 equations to model different mechanisms occurring over different temperature ranges. The kinetic parameters were adjusted using their respective Differential Scanning Calorimetry (DSC) results which found that the rate determining steps

during the reaction changed at different temperatures corresponding to different mechanisms. A more detailed mechanism was developed by Baijot et al. [4] involving phase changes, ambient oxygen effects, reaction steps and the impact of alumina. The reaction itself was the main focus in these papers and not the setup of the powders (pellets, burn tubes). The assumed arrangement of the reactants were arranged as CuO deposits in an aluminum matrix or a core-shell structure of CuO surrounded by aluminum.

Other researchers have taken an engineering approach to better understand the aggregate effects of nanothermite powder or pellet combustion. In this context, the intrinsic chemical mechanisms are of secondary importance compared to the coupled multi-physics interaction for the reactive front propagation. To augment their experimental findings, Nicollet et al. [22] and Stacy et al. [27] used the heat equation to contrast the expected thermal behaviour as opposed to their findings. Kim [17] used a 1D heat transfer model to analyze nano and micro scale Al/MoO_3 thermites, which supported experimental findings of more dense pellets. The reaction details were simplified into a single source term in the heat equation with a reaction progress variable. Knapp et al. [18] recently used their developed Hot Spot model to capture propagation rates in micron thermites based on equivalence ratio and particle sizes. Although these researchers have taken a meta-scale approach to model the combustion, porosity introduces a mode of convective heat transfer to occur within the pellet which they have not addressed.

Chapter 3

Combustion Model and Non-dimensional Analysis

Nanothermite combustion is a complex heat and mass transfer problem which would require extensive information about the heat transfer mechanisms, chemical mechanism and kinetics as well as thermal properties for accurate modelling. A framework is developed to model, in the continuum regime, the ignition and reaction propagation of a Al/CuO nanothermite pellet and to draw conclusions about the dominant combustion mechanisms. This work differs from the previously mentioned literature models by developing a meta-scale model of the porous pellet with simplified chemical processes. From the data presented in the literature review, assumptions can be made to model the essential processes. In this section, the governing equations are introduced and then a non-dimensional analysis is done to explain how the combustion processes will quantified.

3.1 Governing Equations

3.1.1 Mass

Nanothermite pellets are initially in a solid form due to the aggregation and compression of the nanothermites. Based on the adiabatic flame temperature, the products of most thermite reactions are in liquid and/or gas states clearly indicating this reaction is multi-phase. To simplify this process, a two phase model was adopted to focus on the gas and non-gas phases; termed *gas* and *solid* phases respectively. The reaction equation equivalent of the process is:

$$\mathrm{A_{(s)}} \longrightarrow \mathrm{B_{(s,l)}} + \mathrm{C_{(g)}} \tag{3.1}$$

where A is the *solid* phase pre-combustion, B is the *solid* phase post-combustion and C is the *gas* phase. A visual representation is also given in Figure 3.1.

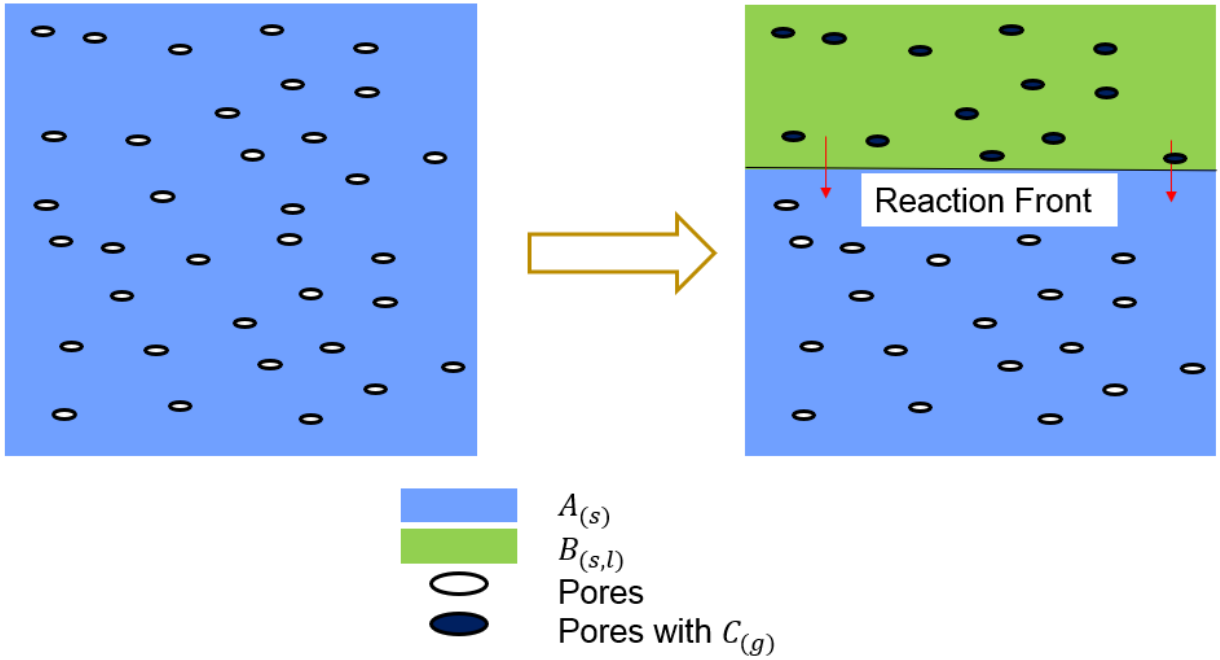

Figure 3.1: 2-phase model progression with reaction front propagation

When converted to a liquid, the resulting density change would require a change in the domain volume as well as the porous nature disappearing. To maintain the porous nature of the pellet while still maintaining some level of thermodynamic accuracy, the thermodynamic behaviour of the liquid and solid states are consolidated into the *solid* phase, but with the mechanical behaviour of solids. Most gases have similar thermal behaviour, so the initial ambient gas already present within the porous material is lumped into the *gas* phase with the gases from combustion. The mass conservation equation for the phases, denoted with the subscripts s (*solid*) and g (*gas*), are:

$$\frac{\partial(\rho_s)}{\partial t} = \dot{\rho}_{s,source} \tag{3.2}$$

$$\frac{\partial(\rho_g)}{\partial t} + \nabla \cdot (\rho_g \mathbf{u}) = \dot{\rho}_{g,source} \tag{3.3}$$

where $\mathbf{u}$ is the vector of the fluid velocity, and $\dot{\rho}_{(g,s),source}$ are the source terms for each phase. At any stage in the reaction (assuming no advection or diffusion of mass), the total mass of each phase has to be conserved. Based on Equation (3.1), the relationship between the source terms is given by:

$$0 = \dot{\rho}_{s,source} + \dot{\rho}_{g,source} \tag{3.4}$$

The derivation of the source terms terms is in section 3.1.4 since these will be closely coupled to the reaction.

3.1.2 Momentum

As the advection of gas within the porous pellet is driven by the pressure gradient resulting from the nanothermite reaction, Darcy's law is used to compute the advection velocity:

$$\mathbf{u} = -\frac{K}{\mu}\nabla P \tag{3.5}$$

where P is the pressure, K is the permeability of the solid, and μ is the viscosity of the gas. Darcy's law governs steady flows through porous media by considering the heterogeneous, porous structure as a homogeneous medium with effective properties.

The permeability in Equation (3.5) is usually experimentally determined for porous media. As there is very limited experimental permeability results for nanothermites pellets, the Kozeny-Carmen equation [16] allows us to relate the porosity of a packed bed of uniform spheres to its permeability for porous structures. The Kozeny-Carmen equation is given by:

$$K = \frac{\phi^3 d_c^2}{k_k(1-\phi)^2} \tag{3.6}$$

where ϕ is the porosity, d_c is the ratio between solid volume and fluid-solid interfacial surface area [23] (will be referred to as characteristic pore size) and k_k is the Kozeny constant. The Kozeny constant is intended to account for information about the flow path, particle shape and connections [23]. This relationship is a standard model for a packed bed of spheres however, in the present model, it permits an order of magnitude estimation of the permeability and resulting advection velocities given the porosity and characteristic pore sizes. More discussion on this will be covered in section 6.2.2.

The pressure gradient driving the advective flow in the Darcy Equation (3.5) is the result of the formation and dilatation of the *gas* due to the reaction. As the *gas* pressure is driving the advective flow, the ideal gas law relating the pressure, density, and temperature is assumed:

$$P = \frac{\rho_g RT}{\phi} \tag{3.7}$$

where R is the specific gas constant. Since the variable ρ_g is per volume of continuum, porosity must be included to reflect the pressure inside the pore. The *gas* and *solid* are assumed to be in thermal equilibrium and thus have equal temperatures.

3.1.3 Energy

The conservation of mass and momentum is supplemented by the total conservation of energy. The kinetic energy of the advecting fluid within the porous media are assumed to be negligible compared to the changes in internal energy of the system. The conservation

of energy is thus given by:

$$\frac{\partial \rho C_{eff} T}{\partial t} + \nabla \cdot (\rho_g \mathbf{u} C_{p,g} T) = \nabla \cdot (\lambda_{eff} \nabla T) + \dot{Q}_{source} \tag{3.8}$$

where $\rho C_{eff} = \rho_s C_{v,s} + \rho_g C_{v,g}$ is the energy storage contribution of the *solid* and *gas* species, $C_{v,i}$ is the specific heat at constant volume for each phase, λ_{eff} is the effective thermal conductivity, $C_{p,g}$ is the specific heat at constant pressure for the *gas*, and $\dot{Q}_{source}$ is heat generated due to the reaction.

3.1.4 Source Terms and Thermal Properties

Modelling the heat released usually involves multiple chemical pathways, however this is not the primary focus of this model. Literature does not have documented reaction steps and their kinetic parameters, so the heat generated from the reaction was assumed to follow an Arrhenius form as was done in Kim [17]:

$$\dot{Q}_{source} = \rho_{s,0} \dot{\eta} \Delta H \tag{3.9}$$

$$\dot{\eta} = A_0 (1 - \eta) \exp\left(-\frac{E_a}{R_u T}\right) \tag{3.10}$$

where $\rho_{s,0}$ is the initial density of *solid*, ΔH is the enthalpy of combustion, A_0 is the pre-exponential factor, η is the reaction progress variable, Ea is the activation energy, and R_u is the universal gas constant. The initial density of *solid* is calculated based on porosity and the TMD, ρ_{max}, by:

$$\rho_{s,0} = (1 - \phi)\, \rho_{max} \tag{3.11}$$

For many thermite combinations, the TMD is documented in [11]. There is some uncertainty for the values of the pre-exponential and activation energy in Equation (3.10) due to a sizeable debate around the exact mechanisms of nanothermite combustion. This equation is commonly accepted for modelling chemical reactions and is simple enough for implementation in this model. Using this equation is intended to compute the functional form of the physics involved, however this will also be addressed in section 6.2.3.

The enthalpy of combustion is documented for stoichiometric thermite mixtures in Fischer and Grubelich [11]. In calculating these values, the reactions begin at 293 K and the final products are in liquid, gas or solid states. For the reactions with liquid products, the enthalpy of combustion includes the enthalpies of fusion for said products. Using the full enthalpy of combustion will overestimate the temperature since the melting of these products are not accounted for in the present model. Therefore, the enthalpy of combustion used in Equation (3.9) should subtract the enthalpies of fusion of the liquid products to more accurately calculate the expected temperature.

Gas is known to be generated by nanothermites from experiments [26, 1] and theory [11, 3]. The origins of which are subject to some debate with oxygen from oxidizer decomposition [15] or metal vapours [3], however pressure has been measured experimentally which is strong evidence of gas generation. From Equation (3.10), the source terms for Equations (3.2) and (3.3) can be derived. Using the *gas* to define the extent of reaction:

$$\eta = \frac{\rho_g - \rho_{g,0}}{\rho_{g,f}} \tag{3.12}$$

where $\rho_{g,0}$ is the amount of *gas* present in the pores pre-combustion and $\rho_{g,f}$ is the amount of *gas* post-combustion, taking the time derivative allows both source terms to be calculated easily by utilizing Equation (3.10) in:

$$\dot{\rho}_{g,source} = \dot{\eta}\rho_{g,f} \tag{3.13}$$

The amount of gas generated is not reported in literature, but the calculations done in Fischer and Grubelich [11] give predicted amounts of gas generated per mass of mixture (examples are listed in Table 1.1), which were used for this model. The definition of η is used to derive the *gas* source term, however the reaction progress is only dependent on Equation (3.10) and the pressure relationship of Equation (3.7) has no impact.

Since the solid and liquid states are lumped into the *solid* phase, the specific heat is calculated based on the those of the solid reactants to the expected liquid products as the reaction progresses. This was modelled by utilizing the reaction progress variable in

calculating the specific heat:

$$C_{v,s} = C_{v,s0}\,(1-\eta) + C_{v,s1}\,(\eta) \tag{3.14}$$

where $C_{v,s0}$ is a mass fraction weighted specific heat of the reactants at 293 K and $C_{v,s1}$ is a mass fraction weighted specific heat of the products at the adiabatic flame temperature. If the products are in the solid and/or liquid state (B phase in Equation (3.1)) at the adiabatic flame temperature, the specific heat is reflected in the value of $C_{v,s1}$. Specific heat capacity of solids and liquids are approximately constant with respect to temperature, so choosing fixed bounds is reasonable. For the *gas* phase, the exact composition is not known, so the specific heat of the *gas* was selected based on likely composition of the gas. The specific gas constant in Equation (3.7) was adjusted to be consistent with the specie tested.

The porous nature and changing composition will have an impact on the effective thermal conductivity. For this model, the effective thermal conductivity was assumed constant and determined based on possible theoretical values. As an example, the effective thermal conductivity can be estimated for a homogeneous two-phase mixture using the mass-fraction contribution of each component. There exists many theories about the effect of porosity on effective properties for specific microstructure arrangements [32, 24], however each method is associated with specific geometric considerations for the pores within the solid matrix. Since the structure of nanothermites is not easily quantified, choosing an appropriate model for thermal conductivity would prove difficult. The results of the simulations will provide the evidence as to whether this assumption is valid. More about this topic will be discussed in Section 6.2.1.

3.2 Non-Dimensional Analysis

Based on the developed set of partial differential equations governing physics of the nanothermite pellet combustion, a non-dimensionalization of the problem that is kinetically and thermodynamically consistent is done. The proposed non-dimensionalization will help

characterize the relative contributions of the heat transfer modes and time scales on the overall combustion.

For the nanothermite pellet combustion, the characteristic thermodynamic variables governing this problem are the adiabatic temperature of reaction, T_{adia}, the ambient pressure, p_∞, and the specific gas constant of the *gas*, R. Note that the adiabatic flame temperature can theoretically evaluated based on the thermophysical characteristics of the fuel and oxidizer; in the present Al/CuO nanothermite combustion, T_{adia} is set to 2844 K. Through the use of the ideal gas Equation (3.7), a characteristic density can be defined:

$$[T_{ref}] = T_{adia}, \quad [R_{ref}] = R, \quad [p_{ref}] = p_\infty, \quad [\rho_{ref}] = \frac{[p_{ref}]}{[R_{ref}][T_{ref}]} \tag{3.15}$$

Additionally, the characteristic length scale, $[L_{ref}]$ of the problem is chosen to be the height of the pellet. The characteristic velocity is then characterized by the advective velocity of the fluid within the porous nanothermite pellet. The characteristic velocity is directly computed from the Darcy Equation (3.5) which yields:

$$[U_{ref}] = \frac{K}{\mu}\frac{[p_{ref}]}{[L_{ref}]} \tag{3.16}$$

where the $\frac{K}{\mu}$ represents the ratio of the permeability, K, over the dynamic viscosity of the gas. The characteristic time scale of the problem is the ratio of the characteristic length to velocity scale: $[t_{ref}] = \frac{[L_{ref}]}{[U_{ref}]}$.

By non-dimensionalizing the set of governing equations, and more particularly the energy conservation Equation (3.8), the Peclet and Damköhler numbers naturally emerge. These dimensionless numbers are used to respectively define the ratio of convective to conductive heat transfer and advective to chemical timescales of the problem. Based on the selected characteristic kinematic and thermodynamic quantities, their definition is

given by:

$$Pe = \frac{[\rho_{ref}][U_{ref}][R_{ref}][L_{ref}]}{\lambda_{eff}} \tag{3.17}$$

$$Da = \frac{[L_{ref}]}{\tau_{chem}[U_{ref}]} = \frac{\mu}{K}\frac{[L_{ref}]^2}{\tau_{chem}[p_{ref}]} \tag{3.18}$$

The τ_{chem} is chosen to be the inverse of the exponential factor in the Arrhenius equation, $1/A_0$. These quantities will be used to characterize the simulation results in Chapter 5.

Chapter 4

Simulation Details and Numerical Implementation

The model present in Chapter 3 requires a numerical framework to obtain a consistent solution. Commercial and academic software packages exist to aid in solving differential equations such as the ones presented in this thesis. These code packages offer many benefits of having different numerical schemes and user defined functions as well as being thoroughly tested. The choice to develop an in-house simulation code was made based on the author's interest and desire to do so. This chapter will outline the numerical methods implemented to solve the proposed model as well as the details of the simulations conducted that will be analyzed in Chapters 5 and 6.

4.1 Simulation Details

4.1.1 Geometry and Constant Parameters

The pellets and burn tubes from experiments are cylindrical in nature, so a two-dimensional axisymmetric implementation was chosen for the simulation domain. In the present work, the properties representing an Al/CuO nanothermite pellet are used although the model

can be generalized to any gas generating nanothermite material. The domain of radius 1 mm, and height of 6 mm is simulated to compare with experiments conducted at the University of Waterloo [25]. Compared to the experiments, the domain is larger in the axial direction in order to obtain a stable reaction propagation velocity in the pellet while minimizing the boundary condition effects. Each simulation was run until at least 80% of the initial pellet had reacted; this ensures a proper averaged flame front velocity. The computational domain is discretized using 1340 and 224 nodes in the axial and radial direction, respectively. This grid size provided an adequate balance between computational efficiency and required resolution. A mesh study will be shown in section 6.1.3 to prove this resolution is appropriate.

The Kozeny constant in Equation (3.6) was selected to be 72 for all simulations since the nature of the pore network is not quantified for nanothermites. The more significant parameters affecting permeability are the characteristic pore size and porosity, so the choice of Kozeny constant is somewhat arbitrary. The amount of gas generated is not reported in literature, but the calculations done in Fischer and Grubelich [11] suggest stoichiometric Al/CuO reaction generates 0.343 g of gas per gram of reactant mix. Therefore, the value of $\rho_{g,f}$ will be $0.343\rho_{s,0}$. Fischer and Grubelich also report the enthalpy of combustion is documented to be $4.07\,\mathrm{kJ\,g^{-1}}$. As the reaction progresses through temperatures of 298 to 2843 K (adiabatic flame temperature), the products of alumina and copper metal are formed that have melting points of 2327 and 1358 K respectively. To accurately reflect the temperature, the value of ΔH used will subtract the enthalpies of fusion of alumina and copper, having values of 1.09 and $0.21\,\mathrm{kJ\,g^{-1}}$ respectively, from the documented enthalpy of combustion.

4.1.2 Parametric Study

The accurate estimation of the thermophysical and combustion properties of the system is needed for experimental validation. A baseline case was performed by setting all thermophysical and combustion properties ($C_{v,g}$, $C_{p,g}$, R, λ_{eff}, μ, d_c, A_0, and E_a) based on the existing literature. In order to characterize the relative importance of these parameters on

the physical phenomena driving the nanothermite combustion, a sensitivity analysis was performed on these variables. The values of the baseline case and parametric study are summarized in Table 4.1. For each thermophysical condition, the porosity of the pellet, ϕ, was varied from 0.1 to 0.9 (corresponding to 90 to 10% TMD respectively). Since experimental results don't use packing densities above 80% TMD [1] and tend to go as low as about 6% TMD [33] when packed lightly, this range of porosity values is appropriate.

Table 4.1: Parameters used in numerical study

Parameter	**Baseline Case**	**Parametric study**
$C_{v,g}, C_{p,g}, R$	$O_{2(g)}(T)$	$Cu_{(g)}(2844K)$, $Al_{(g)}(2844K)$
$dc \times 10^9$ [m]	40	100, 1000
$\mu \times 10^5$ [kg m^{-1} s^{-1}]	1	10, 100
$A_0 \times 10^{-6}$ [s^{-1}]	4.89	0.489, 2.44
E_a [kJ mol^{-1}]	48	70, 80
λ_{eff} [W m^{-1} K^{-1}]	65	1, 100

The exact composition of the gas generated is not known, but some literature [31, 15, 14] has suggested oxygen due to the decomposition of CuO. Aluminum and copper vapour is also possibly present due to the adiabatic flame temperature and the numerical results of Baijot et al. [3]. To address this uncertainty, the species to model the *gas* were that of oxygen, aluminum and copper vapour. The specific heats will be temperature dependent for oxygen, but constant at 2844 K for the others since their states vary between solid, liquid and gas in the simulated temperature range and their gas state values are of interest. The choice of gas species will fix the values of $C_{v,g}$, $C_{p,g}$ and R due to their thermodynamic relationship.

The thermal conductivity was varied to reflect possible dominant heat conduction modes. Since thermal conductivity is assumed to be constant, a combination of two-phase homogeneous mixtures and experimental results were used to select the values. For stoichiometric Al/CuO, the mass fractions of aluminum and copper oxide were used to determine an effective thermal conductivity assuming no pores. The thermal conductivity of aluminum is significantly higher than most metals, so a higher value was also used in the event that the amount and organization of aluminum in the mixture dominates the

conductivity. The measured experimental thermal conductivity of consolidated aluminum pellets by Stacy et. al. [28] was also used.

Between the gas generated by the reaction and the MDM suggested in literature, the viscosity is varied to reflect the order of magnitudes of gases and liquid metals. The baseline uses the gas values due to the model having gas generated during the reaction. Since the products are expected to be in liquid state, using a viscosity value reflecting liquids should be used to observe the effects on the burning of the pellet.

Without knowing the exact shape and organization of the pores, one can gain some intuition for how to determine the characteristic pore size by considering a spherical pore contained in a cubic volume of length equal to the diameter. By considering the volume of the cube and surface area of the pore, the ratio is $1/\pi d_{pore} \approx 0.318 d_{pore}$, which gives the characteristic pore size a close relationship to the actual pore sizes. Nanothermite pellets are a mixture of nano-sized particles, however SEM images show that the agglomerates are closer to micron sized [21]. Therefore, assuming spherical pores, the characteristic pore size ranged from the order of nanometers to micrometers.

The pre-exponential factor taken from [31] was used in the baseline, but smaller values were also used to examine the effect of slower reaction time scales. In Kim [17], the activation energy values were taken from the reaction of nano- to micron-sized aluminum particles in air. Activation energies reported in Stamatis et al. [29] and Ermoline and Schoenitz [9] are significantly higher, however their kinetics model had a few more equations assuming different reaction mechanisms with temperature. The values from Kim [17] were used to span different possible kinetics.

4.1.3 Boundary and Initial Conditions

The computational domain of the nanothermite pellet is shown in Figure 4.1; the boundary conditions and an illustration of the reaction front propagation are also shown. Being an axisymmetric domain, a zero flux boundary condition is enforced along the centre of the pellet. A constant heat flux, to represent the laser heating, is applied over a radius of 0.2

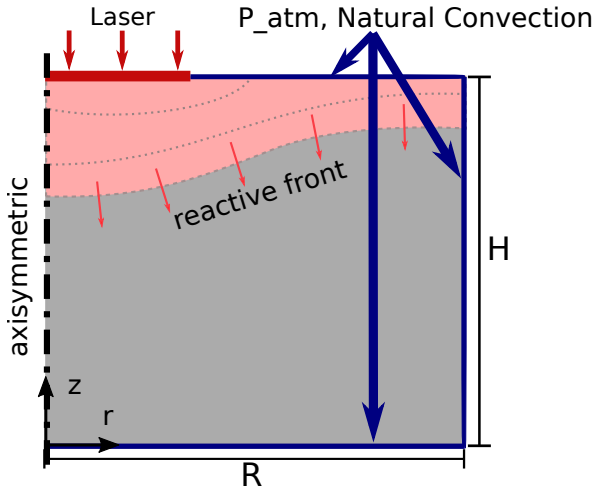

Figure 4.1: Boundary conditions, characteristic dimensions of the simulation with illustration of the propagation of the reactive front

mm of the top boundary at middle of the pellet. The value of the laser power was taken from Saceleanu et al. [25] to be $400\,\mathrm{MW\,m^{-2}}$.

The remaining boundary conditions on the pellet (blue boundaries in Figure 4.1) impose a Dirichlet boundary condition on the pressure. As a result a pressure gradient may develop at the boundary, which permits a mass flux leaving the computational domain; this boundary condition is selected to model the advective mass loss from the pellet to the atmosphere through the porous boundary walls. The thermal boundary conditions allow for natural convection on the pellet walls. The order of magnitude for natural convection of gases is around 1 to $10\,\mathrm{W\,m^{-2}\,K^{-1}}$. Even with this value over an expected temperature difference of 2500 K, the heat loss is less than 1% of the laser flux power used, so it is expected to not have an impact. Nevertheless, a value of $5\,\mathrm{W\,m^{-2}\,K^{-1}}$ was used as the convective coefficient and a free stream temperature of 293 K.

The initial domain temperature is 293 K. For initial conditions, the amount of *solid* present is calculated by Equation (3.11). The initial amount of *gas*, $\rho_{g,0}$, is calculated by Equation (3.7) to ensure the domain begins at atmospheric pressure and an initial temperature 293 K.

4.2 Numerical Implementation

The axisymmetric model is implemented into a numerical framework and the Python-based code has been made accessible on Github (https://github.com/jmreppsUWGrad/2D-Nanothermite) for further use and development. A first-order finite volume method with vertex centred nodes was used to solve the governing equations. The conservation of mass (3.2), (3.3), momentum (3.5) and energy (3.8) equations for the two-phases are solved using finite volume method. This section will outline the relevant concepts of the finite volume method in the current framework as well as details regarding time stepping, stability, boundary and initial conditions, ignition criteria and code progression.

4.2.1 Flux Calculations

The Finite Volume Method is a well established method of numerical solution to partial differential equations, so only the basic principles are outlined here to show how the code operates. A finite volume approximation to Equation (3.3) requires approximating each spatial derivative with a flux function:

$$\frac{\partial}{r\partial r}\left(r\rho_g u\right) \approx \frac{1}{r_{i,j}H_r}\left(m''_{i+\frac{1}{2},j} - m''_{i-\frac{1}{2},j}\right) \tag{4.1}$$

$$\frac{\partial}{\partial z}\left(\rho_g v\right) \approx \frac{1}{H_z}\left(m''_{i,j+\frac{1}{2}} - m''_{i,j-\frac{1}{2}}\right) \tag{4.2}$$

where i and H_r are the node number and control volume length in the radial direction respectively and j and H_z are the node number and control volume length in the axial directions, respectively. To compute the convective face flux in Equation (3.3), a first-order arithmetic average of the properties between nodes are used to approximate the

properties at the control surface:

$$m''_{i+\frac{1}{2},j} = \frac{\rho_{i+1,j} + \rho_{i,j}}{2} r_{i+\frac{1}{2},j} u_{i+\frac{1}{2},j} \tag{4.3}$$

$$m''_{i-\frac{1}{2},j} = \frac{\rho_{i,j} + \rho_{i-1,j}}{2} r_{i-\frac{1}{2},j} u_{i-\frac{1}{2},j} \tag{4.4}$$

$$m''_{i,j+\frac{1}{2}} = \frac{\rho_{i,j+1} + \rho_{i,j}}{2} v_{i,j+\frac{1}{2}} \tag{4.5}$$

$$m''_{i,j-\frac{1}{2}} = \frac{\rho_{i,j} + \rho_{i,j-1}}{2} v_{i,j-\frac{1}{2}} \tag{4.6}$$

where the velocities are directly calculated from discretizing Equation (3.5):

$$u_{i+\frac{1}{2},j} = \frac{K}{\mu} \frac{P_{i+1,j} - P_{i,j}}{\Delta r} \tag{4.7}$$

$$u_{i-\frac{1}{2},j} = \frac{K}{\mu} \frac{P_{i,j} - P_{i-1,j}}{\Delta r} \tag{4.8}$$

$$v_{i,j+\frac{1}{2}} = \frac{K}{\mu} \frac{P_{i,j+1} - P_{i,j}}{\Delta z} \tag{4.9}$$

$$v_{i,j-\frac{1}{2}} = \frac{K}{\mu} \frac{P_{i,j} - P_{i,j-1}}{\Delta z} \tag{4.10}$$

where Δr and Δz are the distances between nodes in the r and the z directions respectively. Since the pressure is calculated at the nodes, a second-order central difference scheme is used to compute the pressure gradient at the control surface which yields a velocity on the control surface requiring no additional interpolation. The same approximation routine applies for the approximation to Equation (3.8):

$$\frac{\partial}{r\partial r}\left(r\rho_g u C_{p,g} T\right) \approx \frac{1}{r_{i,j} H_r}\left(m''_{i+\frac{1}{2},j} h_{i+\frac{1}{2},j} - m''_{i-\frac{1}{2},j} h_{i+\frac{1}{2},j}\right) \tag{4.11}$$

$$\frac{\partial}{r\partial r}\left(r\frac{\partial T}{\partial r}\right) \approx \frac{1}{r_{i,j} H_r}\left(q''_{i+\frac{1}{2},j} - q''_{i-\frac{1}{2},j}\right) \tag{4.12}$$

$$\frac{\partial}{\partial z}\left(\rho_g v C_{p,g} T\right) \approx \frac{1}{H_z}\left(m''_{i,j+\frac{1}{2}} h_{i,j+\frac{1}{2}} - m''_{i,j-\frac{1}{2}} h_{i,j+\frac{1}{2}}\right) \tag{4.13}$$

$$\frac{\partial}{\partial z}\left(\frac{\partial T}{\partial z}\right) \approx \frac{1}{H_z}\left(q''_{i,j+\frac{1}{2}} - q''_{i,j-\frac{1}{2}}\right) \tag{4.14}$$

The diffusion flux functions use second-order central difference schemes to approximate the temperature gradient at the face and are calculated by:

$$q''_{i+\frac{1}{2},j} = \lambda_{eff} r_{i+\frac{1}{2},j} \frac{T_{i+1,j} - T_{i,j}}{\Delta r} \tag{4.15}$$

$$q''_{i-\frac{1}{2},j} = \lambda_{eff} r_{i-\frac{1}{2},j} \frac{T_{i,j} - T_{i-1,j}}{\Delta r} \tag{4.16}$$

$$q''_{i,j+\frac{1}{2}} = \lambda_{eff} \frac{T_{i,j+1} - T_{i,j}}{\Delta z} \tag{4.17}$$

$$q''_{i,j-\frac{1}{2}} = \lambda_{eff} \frac{T_{i,j} - T_{i,j-1}}{\Delta z} \tag{4.18}$$

The enthalpy for the convective terms follow the same interpolation methods (first-order) as seen in the mass flux functions:

$$h_{i+\frac{1}{2},j} = \frac{C_{i+1,j} + C_{i,j}}{2} \frac{T_{i+1,j} + T_{i,j}}{2} \tag{4.19}$$

$$h_{i-\frac{1}{2},j} = \frac{C_{i,j} + C_{i-1,j}}{2} \frac{T_{i,j} + T_{i-1,j}}{2} \tag{4.20}$$

$$h_{i,j+\frac{1}{2}} = \frac{C_{i,j+1} + C_{i,j}}{2} \frac{T_{i,j+1} + T_{i,j}}{2} \tag{4.21}$$

$$h_{i,j-\frac{1}{2}} = \frac{C_{i,j} + C_{i,j-1}}{2} \frac{T_{i,j} + T_{i,j-1}}{2} \tag{4.22}$$

It is worth noting that the values for H_r and Δr are equal in this implementation because the domain is uniformly discretized in the radial direction. In non-uniformly discretized domains, these values would differ due to the contribution of adjacent Δr values on H_r. An example of this in 1D is given by:

$$H_{r,i} = \frac{\Delta r_{i-\frac{1}{2}}}{2} + \frac{\Delta r_{i+\frac{1}{2}}}{2} \tag{4.23}$$

The axial direction is also uniformly discretized, so the same applies for H_z and Δz.

4.2.2 Time Advancement

Since an in-house simulation code was developed, a first-order explicit time scheme was selected as the time advancement scheme due to its easy implementation. Using the time term from Equation (3.2) as an example, the time derivative is discretized as:

$$\frac{\partial(\rho_s)}{\partial t} \approx \frac{\rho_s^{k+1} - \rho_s^k}{\Delta t} \tag{4.24}$$

where k is the time step and Δt is the time step size. In each of the governing equations, all other terms are evaluated at time step k in order to recompute the density or temperature at the time step $k+1$. One drawback to fully explicit time schemes is stability which needs to be addressed. Stability is possible in 2D planar conduction for Fourier numbers:

$$Fo = \frac{\lambda_{eff}\Delta t}{\rho C_{eff}(\Delta r)^2} + \frac{\lambda_{eff}\Delta t}{\rho C_{eff}(\Delta z)^2} < 0.5 \tag{4.25}$$

Convective boundary conditions further restricts the value of the Fourier number to ensure a stable simulation.

In Computational Fluid Dynamics, the Courant-Friedrichs-Lewry (CFL) condition is implemented due to convective terms appearing in the Navier-Stokes equations. Since Equations (3.3) and (3.8) contain a convective term, a modified CFL condition should be considered for stability. Theoretically, stability is possible in 2D flows for CFL numbers:

$$CFL = \frac{u\Delta t}{\Delta r} + \frac{v\Delta t}{\Delta z} < 1 \tag{4.26}$$

where u and v are the fluid velocities in r and z respectively. In this model, the Darcy velocities represent the fluid velocities.

When implementing both CFL and Fo, the Fourier number is more restrictive due to the second order on the discretization, however, the CFL condition is still used should the Darcy velocities become significant. For this thesis, the time step, Δt, was computed using Fourier and CFL numbers of 0.01 to ensure a stable simulation is obtained. Based on these stability constraints, the time step of the simulations ranged between 3×10^{-10}

and 4×10^{-8} s.

4.2.3 Ignition and Burn Rate

Ignition is occurs in experiments when photodiode signals spike or the propagation of the reaction front speeds up and does not require external input. To obtain a self-sustaining reaction, sufficient heat should be generated from the reaction to maintain the reaction front propagation despite heat losses. In this model, the heat generated comes from the source term, $\dot{Q}_{source}$, and ignition will occur when this value exceeds the conductive and convective losses:

$$\dot{Q}_{source} > \nabla \cdot (\rho_g \mathbf{u} C_{p,g} T) - \nabla \cdot (\lambda_{eff} \nabla T) \tag{4.27}$$

Since the equations are implemented numerically, the source term should be a specified factor larger than the losses and should hold in a specified number of control volumes. Once ignition has occurred, the laser flux boundary condition is replaced with the same convective boundary conditions on the other faces. Experimental studies do not report whether their lasers are disabled once ignition occurs, however the reason for doing so in this numerical study is to stop external heating. Keeping the laser flux active adds energy to the domain and likely affect the rate of propagation of the front causing bias in the results and drawing conclusions about the combustion mechanisms.

Estimating the burn rates is usually done using high-speed camera images and manual measurements. After ignition occurs, the instantaneous burn rate is calculated using the reaction progress as seen in Kim [17] at each time step:

$$V_{cw} = \frac{d}{dt} \int_0^{z_{max}} \eta dz \tag{4.28}$$

where z_{max} is the height of the pellet. The average burn rate, $\bar{V}_{cw}$, is then an arithmetic average of the instantaneous burn rates over all time.

4.2.4 Solver Procedure

When the code is initialized, a series of declarations are done as illustrated in Figure 4.2. The domain object contains the arrays of variable data (energy, pressure, densities), discretizations and functions to calculate thermal properties. The solver object contains the functions to solve the governing equations by manipulating the variables directly in the domain object. Multiple cores are implemented using Message Passing Interface (MPI) to speed up the solving process by splitting the domain into equal sized sections that each process focuses on.

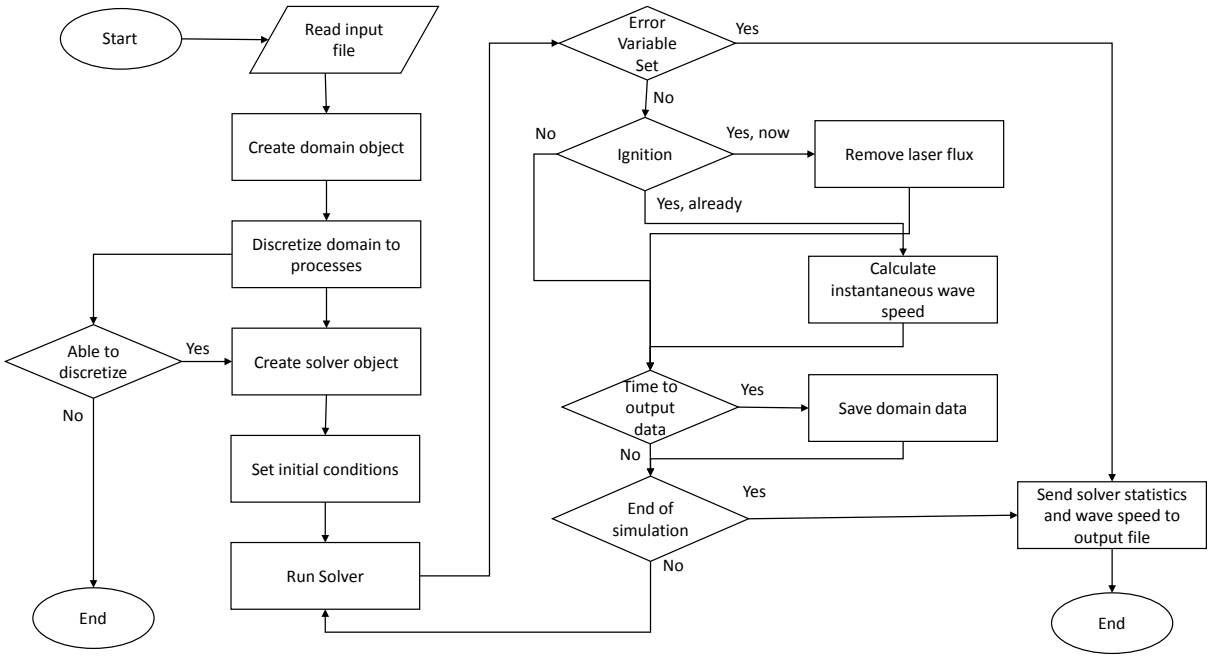

Figure 4.2: Flowchart of simulation code procedure

Inside the 'Run Solver' box of Figure 4.2, equations (3.2), (3.3) and (3.8) are solved in a logical procedure to ensure a consistent solution. A flow chart of this procedure is given in Figure 4.3.

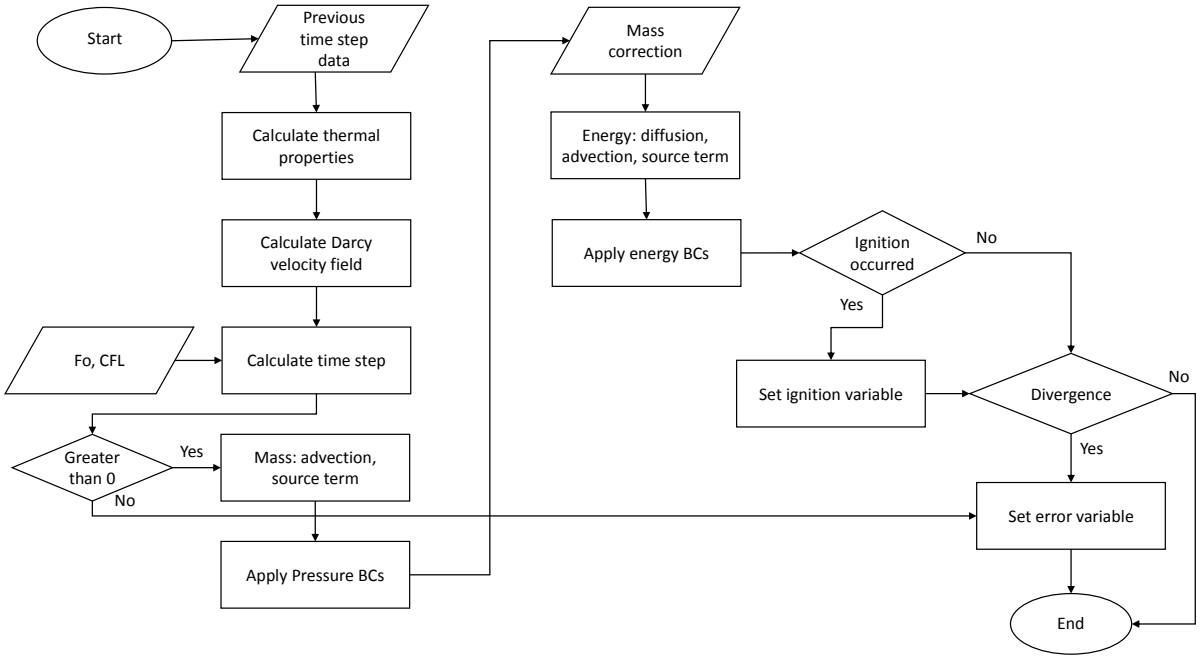

Figure 4.3: Flowchart of 'Run Solver' operation

The temperature-dependent thermophysical properties and the Darcy velocity fields are re-computed at the start of each time step and are assumed constant over the small, Δt of time-advancement step. Similarly, the source terms for the energy and mass equations are computed at the start of the time-step. Using the computed source terms and velocity field, the conservation of mass is then applied. The momentum equation is used directly in the computation of the mass conservation. The boundary conditions are then applied on the pressure field which sets the ambient pressure of the combustion. As the thermodynamic conditions are fully prescribed at the external bounds of the pellet, mass advection at the boundary nodes is necessary to enforce the pressure and density. This permits the advective mass loss through the porous boundaries of the nanothermite pellet and maintains a consistent numerical boundary condition in the problem. The energy equation is then solved by applying the diffusion and advection for both phases. The laser heating and natural convection with the ambient boundary conditions are applied last.

After computing the updated values, if ignition has not occurred previously, the conditions outlined in section 4.2.3 are checked. If the conditions are satisfied, the laser flux boundary condition is replaced with a natural convection boundary condition outlined in section 4.1.3. If ignition occurred previously, the instantaneous burn rate is calculated and the average burn rate is updated.

The divergence check in Figure 4.3 is intended to catch any signs of instability or non-physical values in the domain. Conditions checked include the temperature becoming undefined or negative and the reaction progress is outside the bounds $0 \leq \eta \leq 1$. If the divergence checks are triggered or the calculated time step is negative, the solver box is terminated and an error sent to the main code loop where the 'Error Variable Set' box in Figure 4.2 will terminate the rest of the code safely.

Chapter 5

Results

Following the numerical implementation in Chapter 4 of the model in Chapter 3, the results and important findings are summarized in this chapter. More interpretations about the results, limitations and uncertainty will follow in Chapter 6.

5.1 Burning Regimes

The results of the numerical study confirm the observations from experimental studies that there exists convection or conduction dominated burning regimes, primarily characterized by the density. In less dense pellets, burn rates are significantly higher; with convection being the primary propagation method and sustaining the higher burn rate [25, 8]. This is first demonstrated in the plots seen in Figure 5.1 which show a non-linear relationship between the burn rate and packing density. Thermal conductivity and viscosity have significant impacts on the burn rate of low density pellets where as the characteristic pore size affects all density ranges. Since advection is not significant at high densities, viscosity should not be as important, however the characteristic pore size still has an impact on burn rate. There is also shows a significant impact of the reaction kinetics on the burn rate, but not the state of the *gas*.

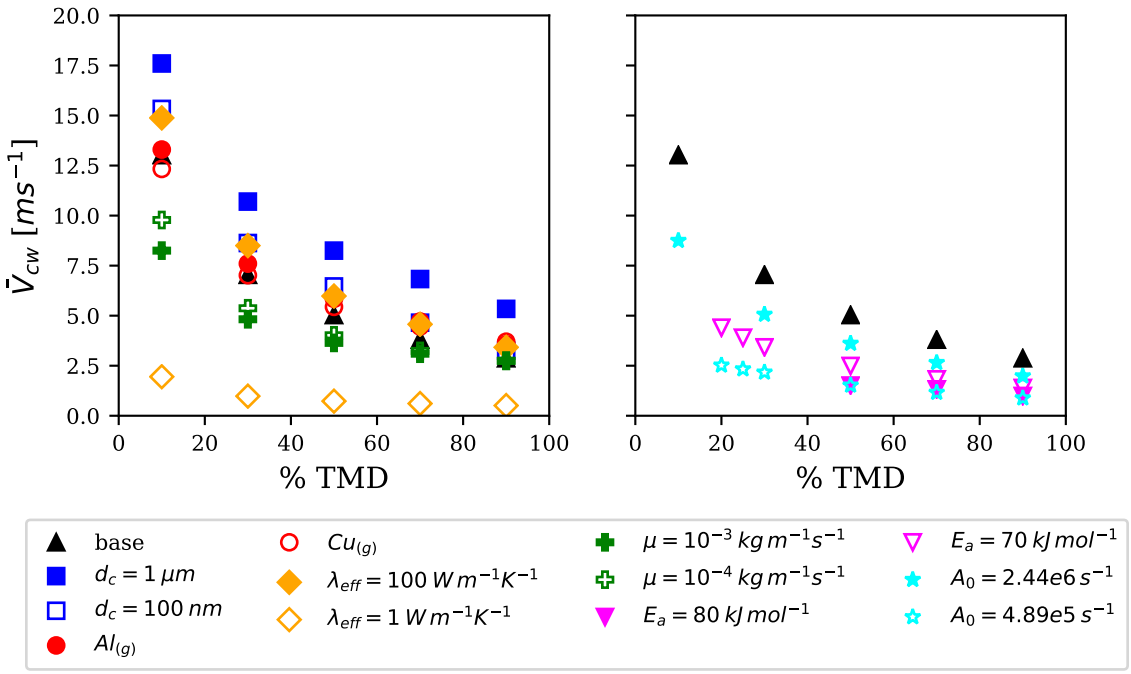

Figure 5.1: Burn rate versus packing density for all simulation data

This relationship is further quantified with the Peclet number which would be expected to increase with decreasing packing density to reflect the larger impact of advective heat transfer as compared to conduction. The derived definition of Peclet (see section 3.2) contains the Darcy velocity and effective thermal conductivity which are characteristic for each heat transfer mode. Figure 5.2 illustrates clearly that Peclet number increases exponentially with packing density. At higher densities, conduction would play a more important role than convection which dominates at lower densities. Also, the thermal state of the *gas* and kinetic parameters do not have an impact on the propagating mechanisms.

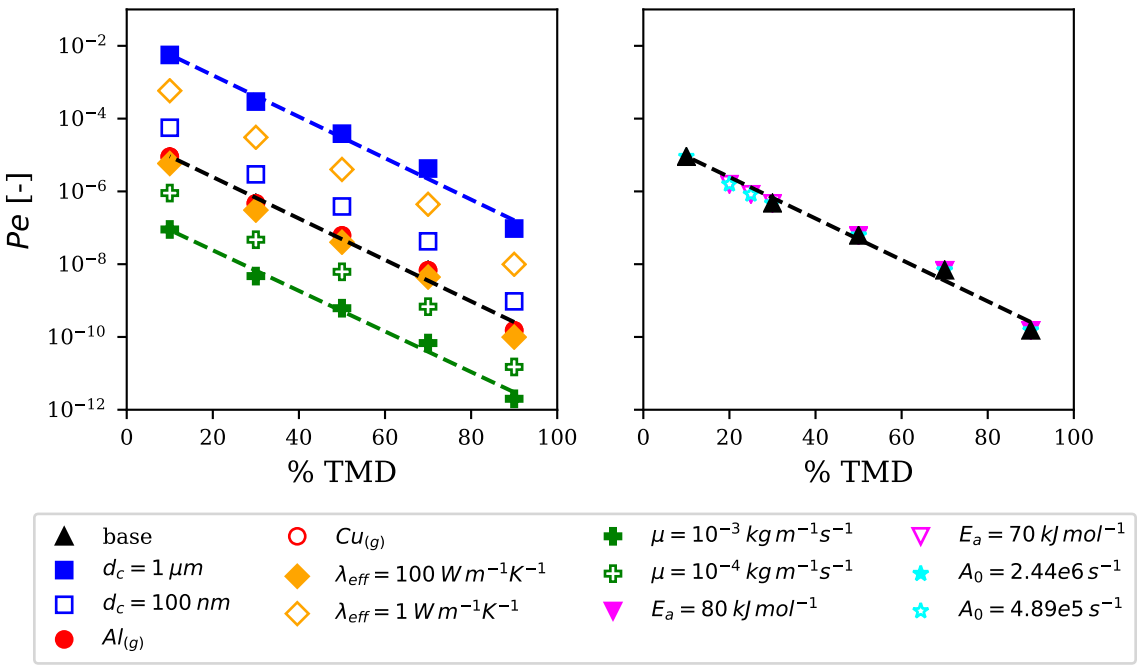

Figure 5.2: Peclet number versus packing density for all simulation data and curve fits for 3 cases

Each of the data points for each parameter study in Figure 5.2 can be fit to an empirical equation with the form:

$$ln(Pe) = A + B(\%TMD) \tag{5.1}$$

The resulting coefficients and correlation coefficient for each parameter changed from the baseline case (Table 4.1) are listed in Table 5.1. All slopes are around -0.131 with the correlation coefficient near 1 except when activation energy is altered, which confirms exponential trends. The resulting fitted curves for 3 of the tested runs are shown in Figure 5.2. More discussion regarding the effect of each parameter seen in Figures 5.1 and 5.2 will be discussed in sections 6.2.1, 6.2.2 and 6.3.

Table 5.1: Regression equation and correlation coefficients according to equation (5.1) for Peclet versus packing density for each parameter case

Parameter Study	A	B	R^2
base	-10.3	-0.131	0.999
$dc = 100\,\mathrm{nm}$	-8.46	-0.131	0.999
$dc = 1\,\mu\mathrm{m}$	-3.85	-0.131	0.999
gas=$Al_{(g)}$	-10.3	-0.131	0.999
gas=$Cu_{(g)}$	-10.3	-0.131	0.999
$\lambda_{eff} = 1\,\mathrm{W\,m^{-1}\,K^{-1}}$	-6.11	-0.131	0.999
$\lambda_{eff} = 100\,\mathrm{W\,m^{-1}\,K^{-1}}$	-10.7	-0.131	0.999
$\mu = 10^{-4}\,\mathrm{kg\,m^{-1}\,s^{-1}}$	-12.6	-0.131	0.999
$\mu = 10^{-3}\,\mathrm{kg\,m^{-1}\,s^{-1}}$	-15.0	-0.128	0.998
$E_a = 70\,\mathrm{kJ\,mol^{-1}}$	-10.7	-0.126	0.951
$E_a = 80\,\mathrm{kJ\,mol^{-1}}$	-8.83	-0.150	0.842
$A_0 = 2.44 \times 10^6\,\mathrm{s^{-1}}$	-10.3	-0.131	0.999
$A_0 = 4.89 \times 10^5\,\mathrm{s^{-1}}$	-10.7	-0.126	0.951

Given the Darcy velocity characterizes the advection portion of the Peclet number, this should be small in densely packed pellets and significant in less dense pellets. When calculating the Darcy velocity, porosity has an exponential effect on the permeability which is a distinguishing factor across each set of data points. Referring to the velocity contours for the baseline at 90 and 10% TMD shown in Figure 5.3, this effect is confirmed since the velocities are small at 90% TMD and distinguishable at 10% TMD. In these contours, the reaction wave is near the middle of the pellet.

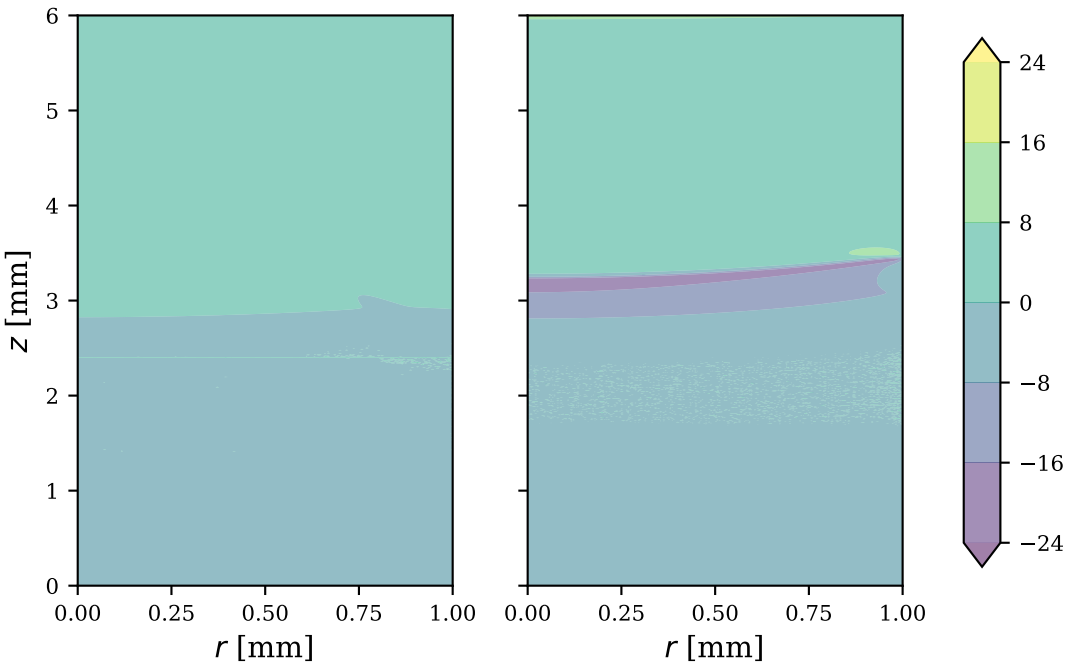

Figure 5.3: Axial Darcy velocity contours for 90% (left) and 10% TMD (right; units $\mathrm{m\,s^{-1}}$)

The contours in Figure 5.3 are a snap shot of the reaction front propagation when it has reached its steady burn rate. Once ignition occurs, the burn rate varies with time until a steady burn rate arises. Figure 5.4 shows the transient burn rate data for the baseline runs where more information about advection can be found. Since the ignition time, burn rate and, thus ending time varies for all cases, these are used to non-dimensionalize time to show the evolution between ignition and final time. An interesting observation is that at lower densities, it takes longer to achieve the steady burn rate. Before ignition, the main propagation mechanism is conduction since little *gas* is generated to augment propagation. Once ignition occurs, *gas* begins to generate at a faster rate and then contributes to a faster burning rate where the advection velocity is sufficiently high (at lower densities). The dashed curve plotted in Figure 5.4 shows the approximate transition from conduction to advection burning. For densities of 50% TMD and higher, the steady burn rate is

achieved faster since the permeability inhibits advection and thus only conduction occurs.

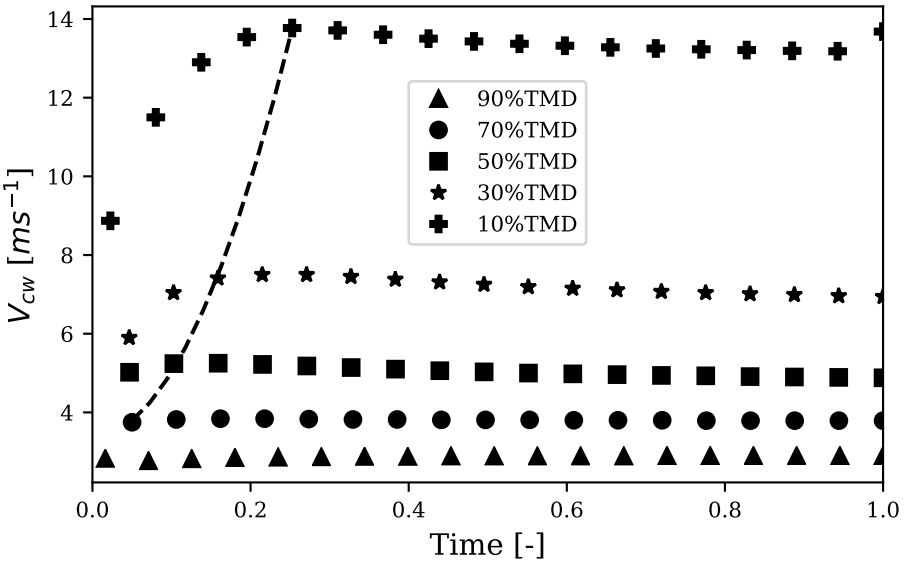

Figure 5.4: Transient burn rate data for baseline cases

Further to regimes, all simulation results show a strong dependence of the burn rate to the Peclet number. Higher Peclet numbers indicate advective heat transfer dominates combustion which is analogous to lower packing densities, however these results show that lower Peclet numbers result in higher non-dimensional burn rates. Non-dimensionalizing the average burn rate ($V^*_{cw} = \bar{V}_{cw}/U_{ref}$), Figure 5.5 shows a predictable, but unexpected trend of burn rate for a given Peclet number. The major contributors to this trend are the flow and conduction determining parameters while the kinetic parameters collapse to the same region as the baseline. While there is a clear relationship with Peclet number and non-dimensional burn rate, there is a significant deviation between the lowest and highest thermal conductivity cases. Although the definition of Peclet number has thermal conductivity in its definition, the Peclet number, alone, cannot be used to characterize the transport phenomena occurring. In this study each parameter is treated as independent, however in reality the thermal conductivity and characteristic pore size would be related

through the nature of the pore structure. More will be discussed in section 6.2.1 and 6.2.2. Once again, the thermal state of the *gas* is indistinguishable from the other parameters.

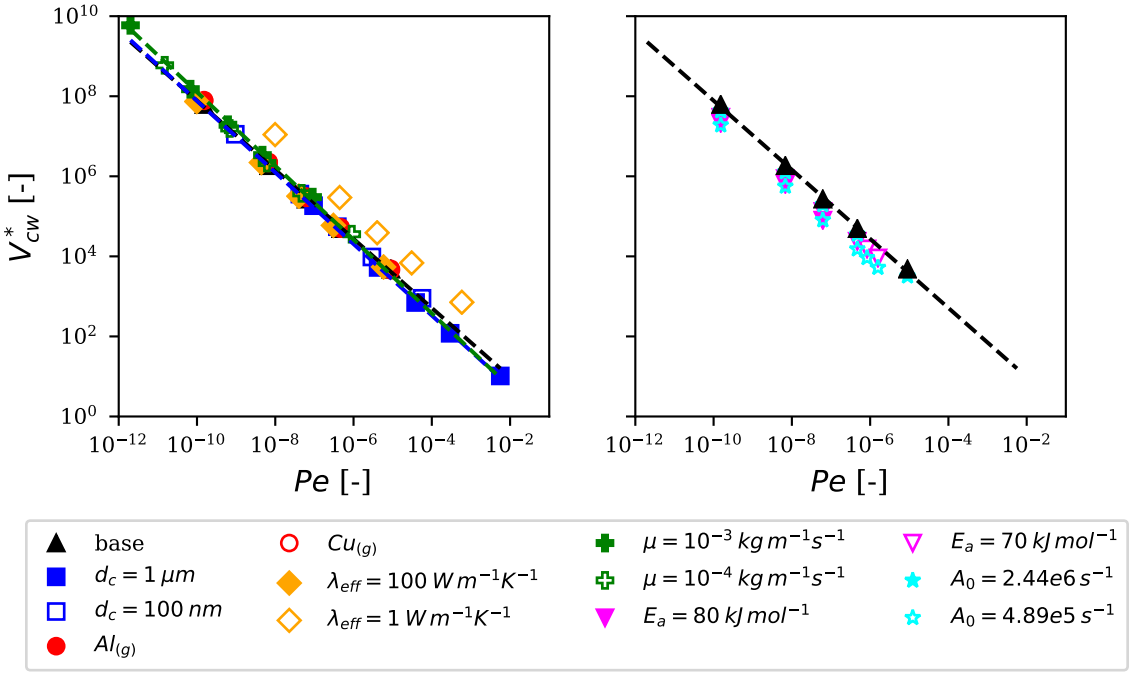

Figure 5.5: Non-dimensional burn rate versus Peclet number for all simulation data and curve fits for 3 cases

The data in Figure 5.5 can be fit to an empirical equation with the form:

$$\log(V^*_{cw}) = A + B\log(Pe) \tag{5.2}$$

The slopes are listed in Table 5.2 and fit well at -0.88 with R^2 consistently close to 1. More discussion regarding this relationship are in sections 6.1.3

Table 5.2: Regression equation and correlation coefficients according to equation (5.2) for non-dimensional burn rate versus Peclet number for each parameter case

Parameter Study	A	B	R^2
base	-1.71	-0.863	0.979
$dc = 100\,\mathrm{nm}$	-1.71	-0.859	0.989
$dc = 1\,\mu\mathrm{m}$	-2.42	-0.893	0.988
gas=$Al_{(g)}$	-1.90	-0.882	0.987
gas=$Cu_{(g)}$	-2.12	-0.893	0.980
$\lambda_{eff} = 1\,\mathrm{W\,m^{-1}\,K^{-1}}$	-0.213	-0.882	0.967
$\lambda_{eff} = 100\,\mathrm{W\,m^{-1}\,K^{-1}}$	-1.96	-0.866	0.982
$\mu = 10^{-4}\,\mathrm{kg\,m^{-1}\,s^{-1}}$	-2.01	-0.885	0.974
$\mu = 10^{-3}\,\mathrm{kg\,m^{-1}\,s^{-1}}$	-2.55	-0.921	0.942
$E_a = 70\,\mathrm{kJ\,mol^{-1}}$	-2.62	-0.873	0.990
$E_a = 80\,\mathrm{kJ\,mol^{-1}}$	-4.11	-0.929	1.0
$A_0 = 2.44 \times 10^6\,\mathrm{s^{-1}}$	-2.078	-0.864	0.984
$A_0 = 4.89 \times 10^5\,\mathrm{s^{-1}}$	-3.24	-0.881	0.993

5.2 Reaction Kinetics and Ignition Delay

Of the literature examined, only Saceleanu et al. [25] reported the ignition delay which they defined as the time before the reaction front was formed as confirmed by high speed images and photodiode detection of intermediate species. The numerical results presented here in Figure 5.6 support their findings as far as the linear behaviour with respect to packing density. The slope is less steep and about one order of magnitude smaller (Saceleanu et al. [25] reported ignition delays greater than 1 ms for stoichiometric Al/CuO). Al/MoO_3 pellets tend to show ignition delays on the order of 10 to 100 ms [13, 27]. More discussion about ignition delay is continued in section 6.1.2.

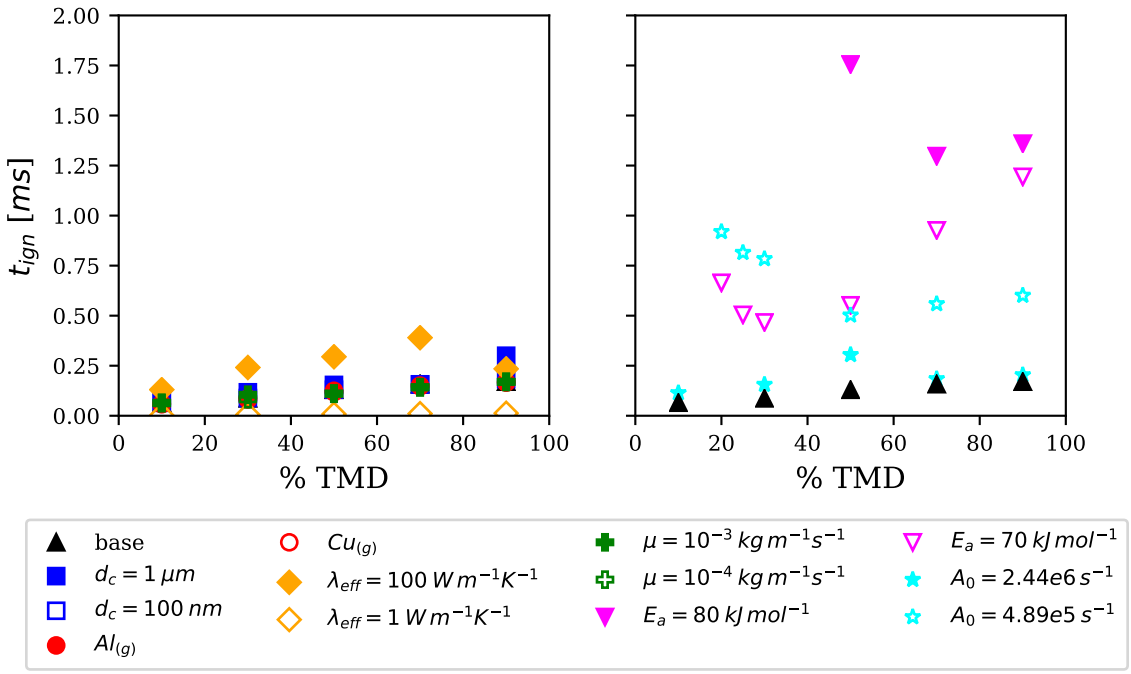

Figure 5.6: Ignition delay versus packing density for all simulation data

In Figure 5.6, an interesting trend appears when the reaction parameters are changed. For all other parameter changes, the ignition delay is consistently higher at densely packed pellets, however a local minimum in ignition delay appears at higher activation energies and low pre-exponential values. Data points are missing for both activation energy studies as well as the lower pre-exponential factor case because ignition in the model was not achieved for those packing densities. From Figures 5.1, 5.2 and 5.5, only ignition delay is significantly affected by these parameters. More discussion will follow in section 6.2.3.

Another comparison of the chemical kinetics can be made using the Damköhler number. The derived definitions (outlined in section 3.2) use the Darcy velocity and pre-exponential factor to define the relative time scales. At lower densities, the advection velocity is expected to be higher due to the ease of flow within the porous pellet. Figure 5.7 shows this trend is exponential in nature regardless of the inputs which further supports the

burning regimes observed.

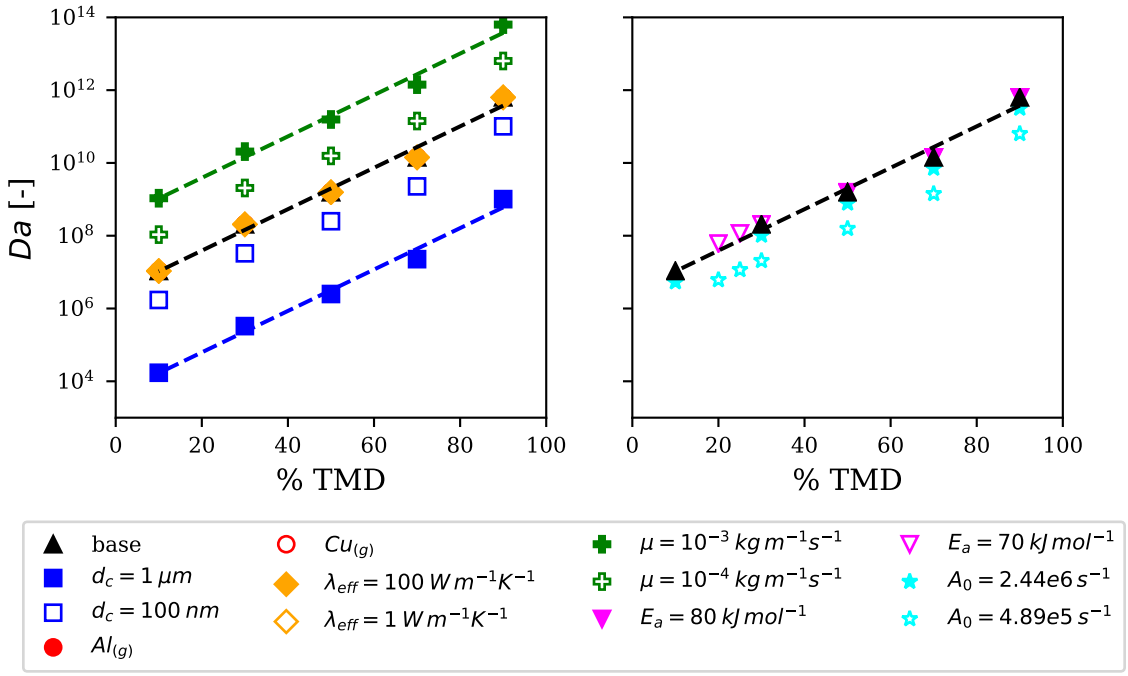

Figure 5.7: Damköhler number versus packing density for all simulation data and curve fits for 3 cases

Following a similar empirical fit done for the Peclet number and packing density (equation (5.1)), Table 5.3 shows the slopes are equal in magnitude to those of the Peclet number trends. Since the Peclet number is proportionate to the reference velocity and the Damköhler number is inversely proportionate, the slopes should only be negatives multiples. Based on the R^2 values, the correlation is not fully consistent with equation (5.1).

Table 5.3: Regression equation and correlation coefficients according to equation (5.1) for Damköhler versus packing density for each parameter case

Parameter Study	A	B	R^2
base	14.9	0.131	0.790
$dc = 100\,\mathrm{nm}$	13.0	0.131	0.790
$dc = 1\,\mu\mathrm{m}$	8.42	0.131	0.790
gas=$Al_{(g)}$	14.9	0.131	0.790
gas=$Cu_{(g)}$	14.9	0.131	0.790
$\lambda_{eff} = 1\,\mathrm{W\,m^{-1}\,K^{-1}}$	14.9	0.131	0.790
$\lambda_{eff} = 100\,\mathrm{W\,m^{-1}\,K^{-1}}$	14.9	0.131	0.790
$\mu = 10^{-4}\,\mathrm{kg\,m^{-1}\,s^{-1}}$	17.2	0.131	0.790
$\mu = 10^{-3}\,\mathrm{kg\,m^{-1}\,s^{-1}}$	19.5	0.131	0.790
$E_a = 70\,\mathrm{kJ\,mol^{-1}}$	15.26	0.126	0.745
$E_a = 80\,\mathrm{kJ\,mol^{-1}}$	13.4	0.150	0.916
$A_0 = 2.44 \times 10^6\,\mathrm{s^{-1}}$	14.2	0.131	0.790
$A_0 = 4.89 \times 10^5\,\mathrm{s^{-1}}$	12.95	0.126	0.745

Chapter 6

Discussion

In order to obtain the results presented in Chapter 5, certain assumptions were made in deriving the model which were covered in Chapter 3. As a follow up, a discussion regarding these assumptions, uncertainty in the quantities and implementation as well as the relation to other literature studies will be conducted.

6.1 Modelling Error

6.1.1 Assumptions and Errors

Porous media can be modelled as a continuum or with a pore-scale model. At the pore-scale, the governing fluid flow equations can be solved accounting for changing pore sizes and connections. Since the equations for each pore are solved, computational limitations will restrict the number of pores that can be reasonably simulated. Using Darcy's law is a continuum regime approach which assumes a homogeneous composition with effective properties accounting for the pores. The details of the pore structure, size and connection are removed with this approach, however computational efforts are not as restricted.

As previously stated in section 3.1.1, the expected combustion temperatures should consume the pellet yielding liquid and gas products which does not leave a solid structure

left to model. With that said, the intention is to model the propagation mechanisms due to the porous nature of the pellet. The unreacted portion is reasonably modelled whereas the reacted portion will be very wrong due to the non-solid state. With changing states, properties like thermal conductivity and viscosity will also change due to changing composition (reactants versus products) and thermodynamics. Specific heat was varied for the *solid* phase to attempt to maintain some thermodynamic consistency, however thermal conductivity and viscosity are maintained as specified constants.

6.1.2 Burn Rate and Ignition Delay

Given that an instantaneous and average burn rate are calculated, an appropriate average burn rate will result when the instantaneous burn rate converges to the averaged value. All simulation runs show various transient instantaneous burn rates early during combustion, but do stabilize near their arithmetically averaged burn rate. The previously shown Figure 5.4 shows evidence that the instantaneous burn rate does converge to the average values.

The way in which ignition delay is defined varies, to a degree, in literature, however, in this numerical implementation, it is defined as when the heat released is an order of magnitude higher than the conduction and advection heat losses. Material ablation in laser ignited nanothermite pellets can have an impact on ignition delay. This was observed in the Al/CuO experiments of Saceleanu et al. [25] and studied in Stacy et al. [27] for Al/MoO_3 nanothermite pellets which found that ignition delay increases when more material is ablated during preheating. Ablation occurs due to a combination of gas generation and thermal expansion of the particle mixtures [27]. The presented model does not account for ablation which is a likely reason why the ignition delays reported in literature and this model differ by an order of magnitude. For this reason, the values of ignition delay are not directly comparable to literature, but the trends can be. Higher density pellets result in more heat released, but also more capacity for heat storage. The laser heats the surface of the pellet where heat diffuses, advects with the gases, leaves via ablation or is stored to raise the temperature. More heat storage requires more heat input to raise the temperature of the pellet in order to ignite the reaction. Therefore, it makes sense that less

dense pellets require less time to ignite when heated by the same powered laser. Keeping ablation as a constant, lower densities require less time to ignite since less heat is required to raise the temperature to its ignition point.

6.1.3 Validation and Verification

Using the experimental data from Saceleanu et al. [25], Weismiller et al. [33], and Ahn et al. [1], the non-dimensionalization techniques presented in section 3.2 can be used to compare their experimental results with the numerical results. The characteristic pore size was calculated used their reported specific surface area of the particles used to synthesize the compounds and the TMD of Al/CuO nano-thermites to obtain an equivalent length scale representing the surface area and volume ratio (more discussion on this in section 6.2.2). Effective thermal conductivity was calculated as a mass fraction mixture of aluminum and copper oxide at the reported equivalence ratios. Weismiller's experiments were done at different ambient pressures, so the reference pressure was changed. From Figure 6.1, the experimental results from Saceleanu are very close to numerical results of this study. Weismiller's data sits at the lower end of Peclet numbers suggesting more convective heat transfer than in Saceleanu's data, however the pressure dependence on the reaction observed by Bazyn et al. [5] is the likely phenomena not accounted for in this model. The burn rates obtained approached $1000\,\mathrm{m\,s^{-1}}$ in Weismiller versus $100\,\mathrm{m\,s^{-1}}$ in Saceleanu. Ahn's data seems to be in line with the thermal conductivity case seen in Figures 5.2 and 5.5.

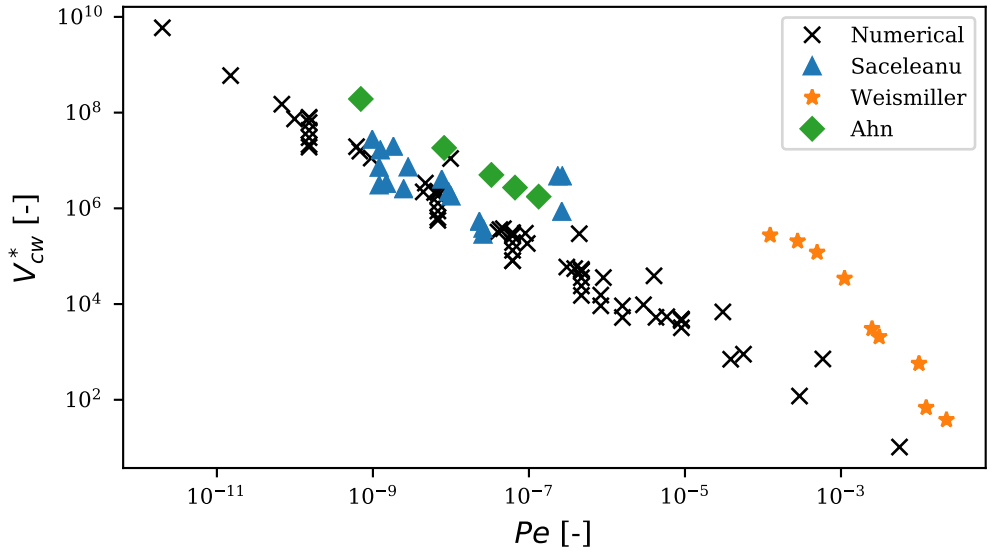

Figure 6.1: Comparison of non-dimensional numerical and experimental results

Pressure has been measured and predicted for Al/CuO nanothermite combustion in previous literature. Sanders et al. [26] measured pressures around 1 MPa for loose powders (about 6% TMD) in a pressure cell and 10 MPa in low density burn tube experiments. Weismiller et al. [33] measured 10 MPa at 6.6% TMD. Baijot et al. [3] also determined the pressure at different stages of Al/CuO reaction between 10 and 100 MPa. The results of this study show peak pressure values between 10 MPa at low densities and 90 GPa at higher densities which is higher than most experiments. At high densities, more gas is generated and the low porosity results in higher pressures modelled (by Equation (3.7)) however, the pellet is likely to disintegrate at these pressures. The transient pressure data for the baseline at 10% TMD is shown in Figure 6.2 which is in good qualitative agreement with the transient pressure data reported in Sanders et al. [26] and Baijot et al. [3]. Therefore, pressure can be predicted with some accuracy for lower densities, but becomes unphysically high at higher densities.

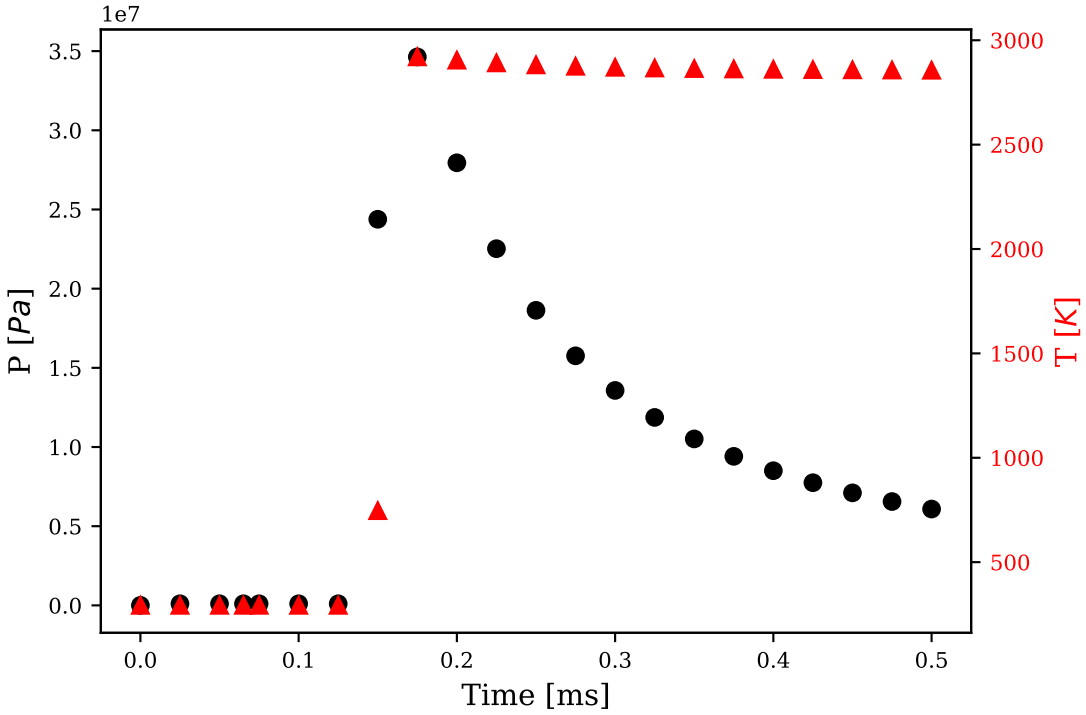

Figure 6.2: Pressure and temperature evolution at 1 mm from the top and 0.5 mm from the centre of the pellet for 10% TMD

The temperature evolution is also plotted in Figure 6.2 which is near the adiabatic flame temperature. According to calculations done in Sanders et al. [26] suggest the adiabatic flame temperature varies with equivalence ratio and Weismiller et al. [33] showed it varies with ambient pressure. The reaction model is too simple to consider these factors, so Figure 6.2 serves as a confirmation that temperatures are not significantly different than the adiabatic flame temperature for stoichiometric reactions from Fischer and Grubelich [11].

A mesh independence study was performed considering the maximum pressure for the parametric study case where $d_c = 1\mu m$ and $\phi = 0.3$. Based on the results presented in Chapter 5, the characteristic pore size has a significant impact on the burn rate, so performing a mesh study where a combination of conduction and convection are occurring

would be a better indicator than where only conduction is dominant. The results are shown in Figure 6.3. All the refined meshes tested greater than 100 000 nodes tend to converge to the same value within 1% which confirms that the chosen mesh of about 300 000 nodes is appropriate for all the simulations results.

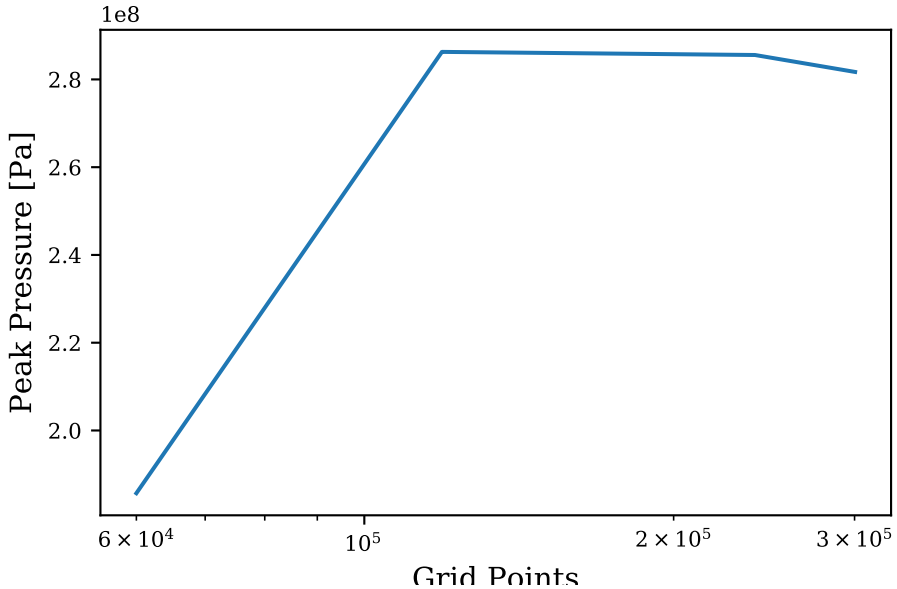

Figure 6.3: Mesh study for maximum pressure

6.2 Uncertainty of Properties

6.2.1 Thermal Conductivity

Based on the results in Figures 5.1, 5.2, 5.5 and 5.7, there is a strong dependence on thermal conductivity. The case where the value from Stacy et al. [28] for compact aluminum pellets seems to trend similar to the data from Ahn et al. [1] shown in Figure 6.1. Conduction is generally accepted as the propagation mechanism for dense pellets whereas convection tends to dominate in less dense setups. When non-dimensionalizing the experimental data

in Figure 6.1, thermal conductivity is estimated using the equivalence ratios reported and assuming no porosity. Despite neglecting porosity, the data from Saceleanu et al. [25] fits the numerical results. The data from Ahn et al. [1] is parallel to the main cluster of data points, and also fits an extension of the low thermal conductivity cases. This would suggest that the thermal conductivity from Stacy et al. [28] is accurate.

For a porous medium, conduction occurs through the solid structure, but becomes impeded at the pores since the thermal conductivity of gases is orders of magnitude smaller than solids. Correlating porosity and effective conductive properties in porous media has been the subject of some literature studies [2, 32, 24] that summarize existing theoretical models. For a given volume fraction of a two-phase mixture, there are accepted upper and lower bounds of thermal conductivity values given by the Parallel and Series conductance formulae:

$$\lambda_e = (1-\psi)\lambda_1 + \psi\lambda_2 \tag{6.1}$$

$$\lambda_e = \left[\frac{1-\psi}{\lambda_1} + \frac{\psi}{\lambda_2}\right]^{-1} \tag{6.2}$$

where λ_e is the effective property, λ_1 is the property of the continuous phase, λ_2 is the property of the dispersed phase and ψ is the volume fraction of the dispersed phase. For porous media, the pores are the dispersed phase and ψ is the porosity. Due to the significant difference in conductivity values for gases and solids, the spread between these bounds are significant. A number of correlations (including the Parallel and Series conductances) from Wang et al. [32] and Askari et al. [2] are plotted in Figure 6.4 using solid and gas thermal conductivities of 100 and 0.01 $\mathrm{W\,m^{-1}\,K^{-1}}$ respectively.

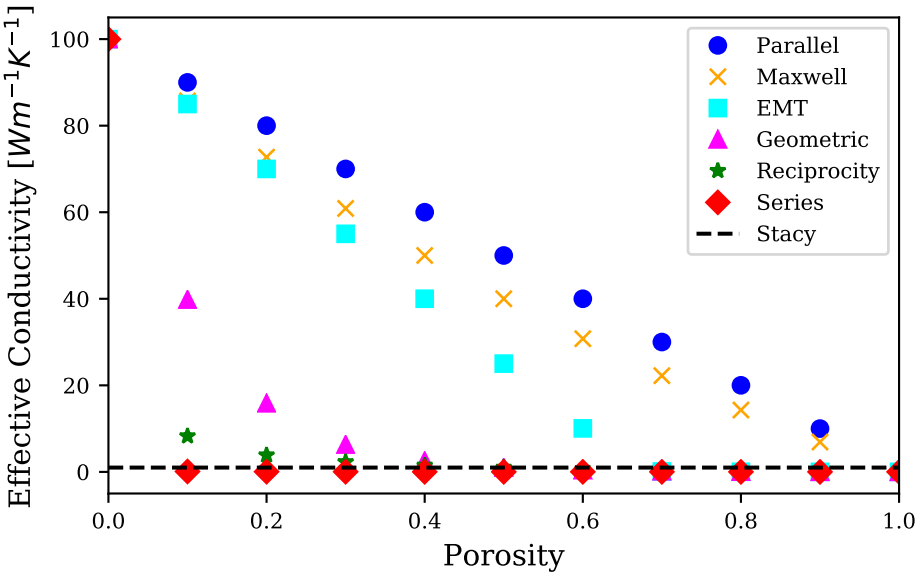

Figure 6.4: Effective conductivity models as a function of porosity

Theoretical models to predict effective properties exist that are derived based on assumptions about the size and distribution of the pores [24]. In general, they can only be used for simple, quantified structures and cannot be used to predict the properties of new materials [32]. The Maxwell relationship was derived for a solid matrix with small, dispersed spherical pores, which was found to be valid for porosities below 25% [24]. The Effective Medium Theory (EMT) assumes a random distribution of each phase and Reciprosity assumes the material is statistically equivalent when switching the volume ratios [32]. With these basic theories, other researchers have modified them with empirical constants or formed combined models. Issues arise due to the increased complexity of forming such networks or due to the material not conforming to the assumptions each model was built on. Most experimental setups have porosities between 0.94 [33] and 0.2 [1] which, at the very least, requires a model that is valid for high volume fractions of the second phase. Without being able to quantify the pore structure for even a first-order approximation, an appropriate thermal conductivity model cannot be chosen responsibly. The maximum observed thermal conductivity measurement by Stacy et al. [28] is shown with horizontal

dashed lines in Figure 6.4 for comparison.

6.2.2 Characteristic Pore Size

Nanothermite pellets are a mixture of nano-sized particles, however SEM images show that the agglomerates are closer to micron sized [21, 25]. The characteristic pore size is the dominant variable in Equation (3.6) to determine the permeability or the ease of flow through the porous pellet. Quantifying the pore structure has not been done in nanothermites and based on Figures 5.1, 5.2 and 5.7 there is significant sensitivity which makes this parameter even more important. Plotting the characteristic pore size, thermal conductivity and base cases from Figure 5.5 in Figure 6.5 shows the relative difference of each. Since the reference velocity is present in the Peclet and non-dimensional burn rate, both groups are equally affected whereas the thermal conductivity effect is mainly on the Peclet number.

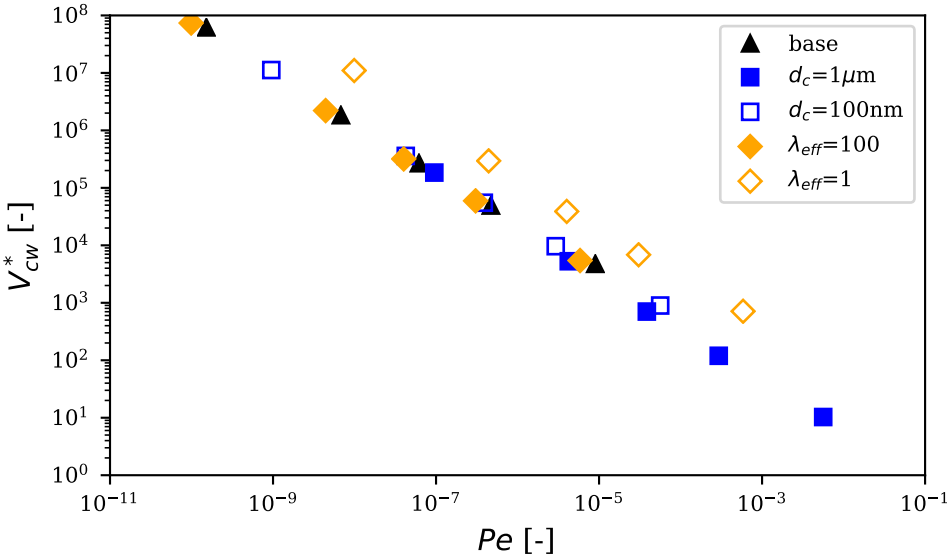

Figure 6.5: Non-dimensional burn rate versus Peclet number for characteristic pore size and thermal conductivity cases

BET specific area is used to quantify the powders used to synthesize the thermites in [1] and [25] which quantifies the surface area of the particles normalized by the mass. This information is for the unmixed powders which are nano-scale whereas the agglomerated mixture can be micron sized [21]. Despite this discrepancy, it can be used as a lower bound since it is a measure of the surface area which is one part of the characteristic pore size. Using this in conjunction with the bulk density, the solid volume to fluid-solid interfacial surface area ratio used for d_c can be estimated. The BET specific areas for the as-received particles reported in Saceleanu et al. [25] and Ahn et al. [1] range between 5 and 50 $\mathrm{m^2\,g^{-1}}$ which would correspond to values of between 4×10^{-9} and 4×10^{-8} m for d_c. Increasing the characteristic pore size of Ahn's data in Figure 6.1 will move the results closer to the lower thermal conductivity result points in Figures 5.5 and 6.5. This would correspond to a decrease in fluid-solid surface area, which occurs if isolated pores become connected. While the Kozeny-Carman Equation has a somewhat exponential trend with respect to porosity which could account for this connectivity occurring, using percolation theory [24] would be more accurate.

The pore structure is key for both the characteristic pore size and thermal conductivity. The assumptions associated with effective thermal conductivity models from literature [2, 32, 24] are around the structure of each phase (or pores) within the heterogeneous medium. This study treats the characteristic pore size and thermal conductivity as independent parameters, however they would be related through the nature of the pore structure. Knowing this structure can identify the characteristic pore size and effective conductivity while this study can provide bounds for possible solutions.

6.2.3 Reaction Kinetics

The chemical kinetic parameters (activation energy and pre-exponential factor) affect the heat and mass generation during combustion. The chemical kinetic parameters do not affect the trends seen in Figure 5.5, however their impact can be seen on the ignition delay in Figure 5.6. The trend is mostly linear with density, however with increasing activation energy, the trend turns exponential. The activation energy and pre-exponential factor were

chosen as an estimate for the reaction mechanism and time scales since various values are used in literature [31, 9, 29]. The largest value intended to be used was $100\,\mathrm{kJ\,mol^{-1}}$, however ignition could not be achieved. Using $80\,\mathrm{kJ\,mol^{-1}}$ allowed ignition to occur and develop the trends seen. The pre-exponential factor and activation energy are used in conjunction with each other, so there is likely a mismatch of the physics with the chosen values that has lead to the ignition problems. Based on the definition of ignition (section 4.2.3), density is directly related to the heat released which needs to surpass the conduction and convection losses. Convection is not expected to have much significance early in the reaction since little gas is generated, so conduction is dominant at these times. It can be concluded then that insufficient mass is present to generate enough heat to sustain the propagation wave. At higher activation energies, the deficiency of mass coupled with higher temperatures required to initiate the reaction, means that the local minimum is moving towards higher densities since more mass is required to generate sufficient heat.

6.3 Other Observations

Although the non-linear relationship in Figure 5.1 is in general agreement with the plots seen in Saceleanu et al. [25] and Ahn et al. [1], the order of magnitude of the burn rates is off at the lower packing densities. The lower bound of burn rates (at higher densities) is around 2 to $4\,\mathrm{m\,s^{-1}}$ [25, 33] which is accurate in these results. The magnitude of burn rates for lower densities are around 100 or $1000\,\mathrm{m\,s^{-1}}$ which is significantly higher than the values reported in this thesis (maximum $17\,\mathrm{m\,s^{-1}}$) which means there are additional factors not not properly reflected in this model.

One of the initial assumptions outlined in section 3.1.1 was modelling the reaction gases as well as pore gases in the *gas* phase due to assumed similar thermal behaviours. Figures 5.1, 5.2, 5.6 and 5.7 all show there is little effect on the type of gas chosen, thus validating this assumption. The values of specific heat for oxygen, aluminum and copper gases at the adiabatic flame temperature are 1230, 770 and $380\,\mathrm{J\,kg^{-1}\,K^{-1}}$ respectively. There is a factor of almost 4 difference between copper and oxygen, yet this does not result in a significant deviation for burn rate, Peclet number or ignition delay.

This model considers advection of gases which have significantly lower density than their liquid counterparts. Convection of condensed phases was specified as a likely mechanism for producing the large burn rates [8] with evidence present in some experiments [20] and suggested as plausible in others [33, 26, 13]. Liquids have larger viscosity values than gases, which Figure 5.2 suggests conduction would be the dominating propagation mechanism and Figure 5.1 show a reduction in burn rate. The density of liquids can be 3 orders of magnitude different from their gaseous equivalents, while viscosities range only 2 orders of magnitude. When comparing the advection term in Equation (3.8) with viscosity in Equation (3.5), there is still 1-2 orders of magnitude that advective heat transfer can be enhanced. Specific heat is higher in liquids, but by less than an order of magnitude, so mass is what will enhance convective heat transfer. Some nanothermite reactions such as Al/NiO do not produce significant amounts of gas which would further reduce the convective heat transfer in this model.

Chapter 7

Conclusions

A continuum model of Al/CuO nanothermite pellet combustion was presented which utilized a two-phase mass model coupled with Darcy's law, and the heat equation. The primary objective was to model the porous medium flow resulting from the porosity of the pellet as well as its effects on the reaction propagation rate. A simplified reaction model was used to approximate the reaction kinetics since this was of secondary concern for this study. A non-dimensional analysis of the model yielded numerics that were used to evaluate the burning regimes of combustion.

The model was solved using a finite volume method and explicit time scheme. A Python code framework was developed to numerically implement this method and is available for other researchers to use.

The results support the experimental observations of conduction and convection burning regimes based on packing density, however fall short on the order of magnitude of the burn rates. Likely causes are inability to model condensed phase heat transfer since densities are larger with relatively similar heat capacities. Despite this, non-dimensionalization of the results and experimental studies show surprising agreement.

Ignition delay trends are similar with literature, however also with lower orders of magnitude. A local minimum in ignition delay with respect to density is observed when changing the reaction parameters suggesting that ignition is a function of mass to ensure

sufficient heat is generated to sustain the reaction propagation. Ablation is one possible reason for this discrepancy due to the heat that is applied by the laser but not used to heat up the pellet to ignition.

Based on the results, the model is most sensitive to the thermal conductivity and nature of the pore structure. Better literature data that quantifies the porous structure will reduce the uncertainty in choosing appropriate values.

7.1 Future Work

The next logical step would be to incorporate a multiphase simulation to account for the condensed phase transport suggested by literature. Since the pellets are porous, including transport of liquid products and coupling with the heat equation will provide a benchmark further confirming that the porous nature of the pellets is crucial to modelling the convective heat transfer in less dense pellets. Literature agrees that convection is the dominant reaction propagation in less dense pellets and most acknowledging it is convection of condensed phases.

References

[1] Ji Young Ahn, Ji Hoon Kim, Jong Man Kim, Deug Woo Lee, Jong Kweon Park, Donggeun Lee, and Soo Hyung Kim. Combustion characteristics of high-energy Al/CuO composite powders: The role of oxidizer structure and pellet density. *Powder Technology*, 241:67–73, 2013.

[2] R. Askari, S. Taheri, and S. H. Hejazi. Thermal conductivity of granular porous media: A pore scale modeling approach. *AIP Advances*, 5(9), 2015.

[3] Vincent Baijot, Ludovic Glavier, Jean-Marie Ducéré, Mehdi Djafari-Rouhani, Carole Rossi, and Alain Estève. Modeling the pressure generation in Aluminum based thermites. *Propellants, Explosives, Pyrotechnics*, 40(3):402–412, 2015.

[4] Vincent Baijot, Djafari Rouhani Mehdi, Carole Rossi, and Alain Estève. A multi-phase micro-kinetic model for simulating aluminum based thermite reactions. *Combustion and Flame*, 180:10–19, 2017.

[5] Tim Bazyn, Herman Krier, and Nick Glumac. Evidence for the transition from the diffusion-limit in aluminum particle combustion. *Proceedings of the Combustion Institute*, 31(2):2021 – 2028, 2007.

[6] Sarah Brotman, Mehdi Djafari Rouhani, Carole Rossi, and Alain Estève. A condensed phase model of the initial Al/CuO reaction stage to interpret experimental findings. *Journal of Applied Physics*, 125(3), 2019.

[7] S. W. Dean, M. L. Pantoya, A. E. Gash, S. C. Stacy, and L. J. Hope-Weeks. Enhanced Convective Heat Transfer in Nongas Generating Nanoparticle Thermites. *Journal of Heat Transfer*, 132(11):111201, 2010.

[8] Garth C Egan and Michael R Zachariah. Commentary on the heat transfer mechanisms controlling propagation in nanothermites. *Combustion and Flame*, 162(7):2959–2961, jul 2015.

[9] Alexandre Ermoline, Mirko Schoenitz, and Edward L. Dreizin. Reactions leading to ignition in fully dense nanocomposite Al-oxide systems. *Combustion and Flame*, 158(6):1076–1083, 2011.

[10] Mark E. Ewing, Travis S. Laker, and David T. Walker. Numerical Modeling of Ablation Heat Transfer. *Journal of Thermophysics and Heat Transfer*, 27(4):615–632, 2013.

[11] S. Fischer and Mark Grubelich. A survey of combustible metals thermites and intermetallics for pyrotechnic applications. In *32nd AIAA Joint Propulsion Conference*, page 15, 07 1996.

[12] Catalin FlorinPetre, Daniel Chamberland, Tommy Ringuette, Sophie Ringuette, Suzanne Paradis, and Robert Stowe. LOW-POWER LASER IGNITION OF ALUMINUM/METAL OXIDE NANOTHERMITES. *International Journal of Energetic Materials and Chemical Propulsion*, 13(6):479–494, 2014.

[13] John J. Granier and Michelle L. Pantoya. Laser ignition of nanocomposite thermites. *Combustion and Flame*, 138(4):373–383, 2004.

[14] Rohit J. Jacob, Dylan J. Kline, and Michael R. Zachariah. High speed 2-dimensional temperature measurements of nanothermite composites: Probing thermal vs. Gas generation effects. *Journal of Applied Physics*, 123(11), 2018.

[15] Guoqiang Jian, Snehaunshu Chowdhury, Kyle Sullivan, and Michael R. Zachariah. Nanothermite reactions: Is gas phase oxygen generation from the oxygen carrier an essential prerequisite to ignition? *Combustion and Flame*, 160(2):432–437, 2013.

[16] M. (Massoud) Kaviany. *Principles of heat transfer in porous media*. Mechanical engineering series. Springer-Verlag, New York, 2nd ed. edition.

[17] Kyoungjin Kim. Computational Modeling of Combustion Wave in Nanoscale Thermite Reaction. *International Journal of Energy and Power Engineering*, 8(7):612–615, 2014.

[18] Sebastian Knapp, Norbert Eisenreich, Stefan Kelzenberg, Evelin Roth, and Volker Weiser. Modelling of Al/MnO2 and Ti/MnO2 Thermite Mixtures. *Propellants, Explosives, Pyrotechnics*, 44(6):706–713, 2019.

[19] Valery I. Levitas, Blaine W. Asay, Steven F. Son, and Michelle Pantoya. Melt dispersion mechanism for fast reaction of nanothermites. *Applied Physics Letters*, 89(7):98–101, 2006.

[20] Valery I. Levitas, Michelle L. Pantoya, and Steven Dean. Melt dispersion mechanism for fast reaction of aluminum nano- and micron-scale particles: Flame propagation and SEM studies. *Combustion and Flame*, 161(6):1668–1677, 2014.

[21] I. Monk, M. Schoenitz, R. J. Jacob, E. L. Dreizin, and M. R. Zachariah. Combustion Characteristics of Stoichiometric Al-CuO Nanocomposite Thermites Prepared by Different Methods. *Combustion Science and Technology*, 189(3):555–574, 2017.

[22] Andréa Nicollet, Guillaume Lahiner, Andres Belisario, Sandrine Souleille, Mehdi Djafari-Rouhani, Alain Estève, and Carole Rossi. Investigation of Al/CuO multilayered thermite ignition. *Journal of Applied Physics*, 121(3), 2017.

[23] Turkuler Ozgumus, Moghtada Mobedi, and Unver Ozkol. Determination of kozeny constant based on porosity and pore to throat size ratio in porous medium with rectangular rods. *Engineering Applications of Computational Fluid Mechanics*, 8(2):308–318, 2014.

[24] K. Pietrak and T. Wiśniewski. A review of models for effective thermal conductivity of composite materials. *Journal of Power of Technologies*, 95(1):14–24, 2015.

[25] Florin Saceleanu, Mahmoud Idir, Nabiha Chaumeix, and John Z. Wen. Combustion Characteristics of Physically Mixed 40 nm Aluminum/Copper Oxide Nanothermites Using Laser Ignition. *Frontiers in Chemistry*, 6:1–10, 2018.

[26] V. Eric Sanders, Blaine W. Asay, Timothy J. Foley, Bryce C. Tappan, Adam N. Pacheco, and Steven F. Son. Reaction Propagation of Four Nanoscale Energetic Composites (Al/MoO3, Al/WO3, Al/CuO, and B12O3). *Journal of Propulsion and Power*, 23(4):707–714, 2007.

[27] S. C. Stacy, R. A. Massad, and M. L. Pantoya. Pre-ignition laser ablation of nanocomposite energetic materials. *Journal of Applied Physics*, 113(21), 2013.

[28] Shawn C. Stacy, Xin Zhang, Michelle Pantoya, and Brandon Weeks. The effects of density on thermal conductivity and absorption coefficient for consolidated aluminum nanoparticles. *International Journal of Heat and Mass Transfer*, 73:595–599, 2014.

[29] D. Stamatis, A. Ermoline, and E. L. Dreizin. A multi-step reaction model for ignition of fully-dense Al-CuO nanocomposite powders. *Combustion Theory and Modelling*, 16(6):1011–1028, 2012.

[30] Kimoon Um, Xuan Zhang, Markos Katsoulakis, Petr Plechac, and Daniel M. Tartakovsky. Global sensitivity analysis of multiscale properties of porous materials. *Journal of Applied Physics*, 123(7), 2018.

[31] Swati M. Umbrajkar, Mirko Schoenitz, and Edward L. Dreizin. Exothermic reactions in Al-CuO nanocomposites. *Thermochimica Acta*, 451(1-2):34–43, 2006.

[32] Moran Wang and Ning Pan. Predictions of effective physical properties of complex multiphase materials. *Materials Science and Engineering R: Reports*, 63(1):1–30, 2008.

[33] M. R. Weismiller, J. Y. Malchi, R. A. Yetter, and T. J. Foley. Dependence of flame propagation on pressure and pressurizing gas for an Al/CuO nanoscale thermite. In *Proceedings of the Combustion Institute*, volume 32, pages 1895–1903. The Combustion Institute, 2009.